J. Fluid Mech. (2021), *vol*. 924, A8, doi:10.1017/jfm.2021.616

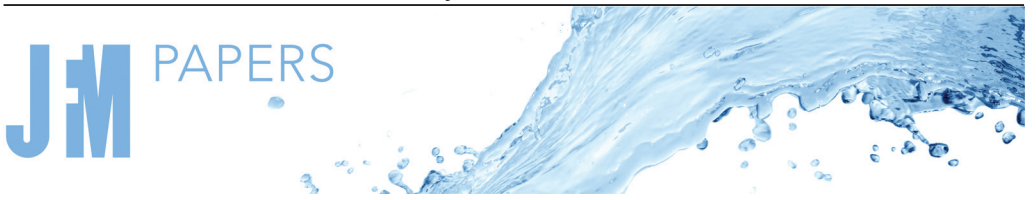

Distributed vortex-wave interactions: the relation of self-similarity to the attached eddy hypothesis

Hugh M. Blackburn[1],†, **Kengo Deguchi**[2],† **and Philip Hall**[2],†

[1]Department of Mechanical and Aerospace Engineering, Monash University, Clayton, VIC 3800, Australia
[2]School of Mathematics, Monash University, Clayton, VIC 3800, Australia

(Received 4 August 2020; revised 31 May 2021; accepted 4 July 2021)

A large-Reynolds-number asymptotic reduction of the Navier–Stokes equations capable of describing a locally periodic vortex-wave array and the associated large-scale variation of the mean-shear velocity field first suggested in Hall (*J. Fluid Mech.*, vol. 850, 2018, pp. 46–82) is extended. The sustaining process of the locally periodic coherent structures is based on the vortex-wave interaction theory of Hall & Smith (*J. Fluid Mech.*, vol. 227, 1991, 641–666), wherein two-dimensional roll–streak fields are supported by localised nonlinear self-interactions of three-dimensional waves that are largest in size within critical layers of the streak field. The variation of the mean velocity is made possible by incorporating a slow change to the mean profile using a Wentzel–Kramers–Brillouin-type approach. As the first extension, we demonstrate that the local structure corresponds to the asymptotic limit of computations in a shearing box. A variety of solutions with different symmetry properties are found via the hybrid numerical asymptotic approach of Blackburn, Hall & Sherwin (*J. Fluid Mech.* vol. 721, 2013, 58–85). Moreover, some solutions show generic flow features such as uniform momentum zones and spatial intermittency known to occur in near-wall turbulent boundary layers. We extend the vortex-wave interaction array theory to show that, in addition to a Reynolds-averaged-Navier–Stokes-type relationship between the large-scale vertical variation of the mean flow and local roll–streak scale, a higher-order analysis gives a second constraint on the slow-scale dynamics. Those constraints are used for the first time to derive the logarithmic law of the wall through a closed asymptotic analysis of self-similar local coherent structures, consistent with the attached eddy hypothesis.

Key words: high-speed flow, critical layers

† Email addresses for correspondence: hugh.blackburn@monash.edu, kengo.deguchi@monash.edu, philip.hall@monash.edu

1. Introduction

This work focuses on coherent structures driven by arrays of nonlinear interactions in shear flows. In particular, by extending the recent work by Hall (2018), henceforth referred to as H18, we establish a relationship between the well-known universal velocity profile present in near-wall turbulent boundary layers and the vortex-wave interaction theory.

Figure 1 is a sketch of the mean velocity profile in a turbulent shear flow as a function of distance from the wall expressed in wall units. Near the wall the mean flow first varies linearly with distance from the wall in the viscous sublayer and then across the so-called buffer layer it evolves into a logarithmic velocity profile. The height at which the buffer layer appears is a function of the friction Reynolds number Re_τ, whereas below the buffer layer the leading-order flow is apparently independent of Re_τ. Further away from the wall in a turbulent boundary layer, the mean part of the flow is thought to be described by von Kármán's 'law of the wall', i.e. the mean velocity varies logarithmically with distance from the wall (von Kármán 1930; Millikan 1938). This logarithmic layer is thicker than the near-wall region and, therefore, capable of supporting a wider range of length scales.

As documented in the recent review paper by Marusic & Monty (2019), a cornerstone of the interpretation of experiments and numerical simulations has been the so-called attached eddy hypothesis due to Townsend (1951). The hypothesis suggests self-similarity within the logarithmic layer, although the hypothesis is based on the assumption that the different eddies of increasing size do not interact, which is unlikely in a highly nonlinear flow. Possible models of the eddy structure which might support that near-wall structure have been advanced by, for example, Perry & Chong (1982) and Perry & Marusic (1995). However, those models, though motivated by particular Navier–Stokes solutions, do not account for how eddies of different sizes might interact.

Since recurrent coherent structures in turbulent wall boundary layers first received attention, the mechanism by which they might be sustained and regenerated has been the subject of much speculation. The interaction between rolls and streaks was an initial dominant theme, with various instabilities proposed as a way to provide recurrence; such works include those of Kim, Kline & Reynolds (1971), Hamilton, Kim & Waleffe (1995), Waleffe (1997), Schoppa & Hussain (2002), Chernyshenko & Baig (2005) and Hwang & Cossu (2011). It was also noted that simplified or restricted numerical models of wall turbulence could provide recurrent structures with many features found in turbulent flows, as observed by Jiménez & Moin (1991), Jiménez & Pinelli (1999), Bakken *et al.* (2005), Flores & Jiménez (2006), Mizuno & Jiménez (2013) and Chung, Monty & Ooi (2014). Cossu & Hwang (2017) concluded from direct numerical simulations that the local streaky structure at any position in the inner layer (see figure 1) self-sustains and indeed persists when the structure in the buffer layer is suppressed. It is noteworthy that uniform momentum zones have also been observed in turbulent near-wall boundary layers by Meinhart & Adrian (1995) and Adrian, Meinhart & Tomkins (2000). More recently, some structural analyses of those uniform momentum zones derived from large Reynolds number simulations suggest that possess hierarchical length scales, possibly related to the attached eddy hypothesis; see de Silva, Hutchins & Marusic (2016), de Silva *et al.* (2017) and Laskari *et al.* (2018). It has also been suggested that a link exists between length scales of uniform momentum zones and balances of terms in the mean momentum equation; see Klewicki *et al.* (2014), Klewicki & Oberlack (2015) and Morrill-Winter, Philip & Klewicki (2017).

It has now become widely accepted that a recurrent interaction between rolls, streaks and waves is implicated in the process by which near-wall coherent structures are sustained in turbulent boundary layers. The interaction of the three key ingredients is described by the

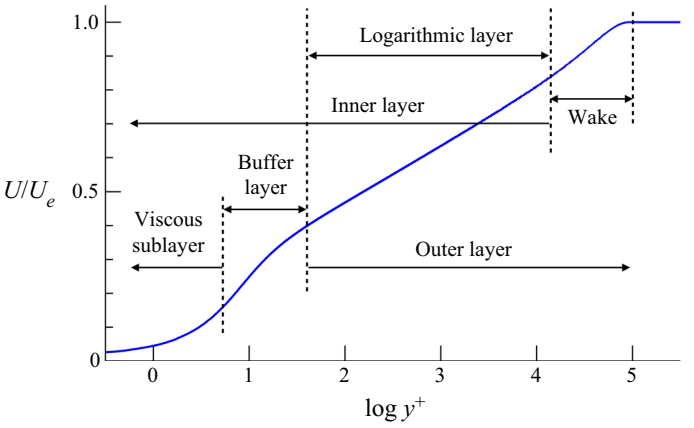

Figure 1. The law of the wall for the mean flow U in turbulent boundary layers. The external mean velocity is U_e and the distance from the wall expressed in viscous wall units is $y^+ = \hat{y}\hat{u}_\tau/\hat{\nu}$ in which the friction velocity based on average wall shear stress $\hat{\tau}_w$ is $\hat{u}_\tau = (\hat{\tau}_w/\hat{\rho})^{1/2}$.

vortex-wave interaction theory, henceforth referred to as VWI, developed by Hall & Smith (1988, 1991), or what in the numerical community is referred to as a self-sustained process (SSP), following the work of Waleffe (1997). In the VWI/SSP approach a wave riding on top of a streak lifted up by a roll feeds energy back to the roll via Reynolds stress to close the cycle. For many years, those two theories had developed independently, until the discovery by Hall & Sherwin (2010) that the VWI interaction equations of Hall & Smith (1991) is the formal large-Reynolds-number asymptotic description of SSP.

The link between the two theories was confirmed by numerical computations of three-dimensional nonlinear finite amplitude solutions of Navier–Stokes equations. At finite Reynolds numbers, numerical investigations of simple canonical flows such as plane Couette flow showed that nonlinear travelling wave or steady solutions typically begin as a saddle-node bifurcation spawning upper and lower branches as the Reynolds number increases (Nagata 1990; Clever & Busse 1992). The SSP description inspired numerous related numerical descriptions of these solutions in channels and pipes by, for example, Waleffe (1998, 2003), Itano & Toh (2001), Faisst & Eckhardt (2003) and Wedin & Kerswell (2004). Moreover, the importance of those solutions in the dynamical systems theory view of turbulence has attracted much attention (Gibson, Halcrow & Cvitanović 2008; Kawahara, Uhlmann & van Veen 2012; Willis, Cvitanović & Avila 2013).

Motivated by the numerically predicted scalings for lower-branch states for Couette flow given by Wang, Gibson & Waleffe (2007), Hall & Sherwin (2010) numerically solved the relevant VWI system for the first time to compare the asymptotic solution with those finite Reynolds number computations. Hall & Sherwin's result, showing that the asymptotic approach described the lower-branch states at Reynolds numbers almost down to the saddle-node point, conclusively demonstrates the clear relevance of the VWI theory to Navier–Stokes dynamics. Moreover, the subsequent finding by Deguchi & Hall (2014*c*) that the upper-branch states are also driven by the same mechanism reinforced the crucial role of the VWI description of high Reynolds number exact coherent structures.

The crucial simplifying feature of the VWI theory is that it enables the Reynolds number to be scaled out of the problem and provides a rational closed interaction system describing the tripartite process allowing rolls, streaks and waves to coexist and support each other.

The process by which the wave interacts with itself to drive the roll through a stress jump across the wave's critical layer is a steady streaming mechanism associated with oscillatory flows (see, e.g. Batchelor 1967, § 5.13). In the first VWI study by Hall & Smith (1988), a Tollmien–Schlichting wave drives the interaction in a viscous wall layer. Subsequently, Hall & Smith (1991) found that the interaction is also possible with an inviscid Rayleigh wave. A key property of the latter type of VWI which differentiates it from classical steady streaming is that in the layer where the oscillatory flow drives a mean flow via Reynolds stresses, this occurs through a jump in stress, rather than in velocity. Thus, the whole interaction process occurs independently of any effects from the walls. Blackburn, Hall & Sherwin (2013) and Deguchi (2015) further showed that, for relatively narrow computational boxes, coherent states in plane Couette flow tend to localise vertically away from any boundaries. They found the localised solutions independently at almost the same time, but each by considering a different asymptotic state.

Blackburn *et al.* (2013) used the VWI equations and showed that the localised states scale like the Kolmogorov 5/3 rule, while Deguchi (2015) used Navier–Stokes equations to find asymptotic equilibrium states at the Kolmogorov microscale. The VWI outcomes of Blackburn *et al.* (2013) were asymptotically matched by full Navier–Stokes computations as confirmed by Deguchi & Hall (2014*a*). When the localised coherent structures found by Blackburn *et al.* (2013) are described in terms of the viscous unit in an unbounded domain, the large asymptotic parameter used in the VWI theory corresponds to the eddy size. Reducing that eddy size towards the Kolmogorov microscale, eventually all terms in the Navier–Stokes equations play important roles and, hence, the asymptotic states described by Deguchi (2015) result. Subsequently, similar localised solutions but attached to the wall have been identified by Eckhardt & Zammert (2018) and Yang, Willis & Hwang (2019), and served as a basis to understand some canonical features of near-wall coherent structures.

A conceptual difficulty in applying the equilibrium states methodologies mentioned above to flows such as turbulent boundary layers is that there is no means of obtaining a range of length and time scales. Thus, in H18 the motivation was to see whether arrays of VWI states are the sustaining mechanism for the more complex states with multiple frequencies.

The approach taken in H18 was twofold. In the first step, the description of VWI states in infinite homogeneous shear flow was derived. This can be done by starting off with an infinite number of vertically localised VWI states as found by Blackburn *et al.* (2013) and moving them closer until they interact. The outcome is VWI states assumed to be periodic in all three directions which, as we shall see in § 2, relate to shearing box studies of homogeneous shear turbulence. The periodic shearing box model has long been used to capture the 'local' turbulent flow properties that arise as a part of more global hydrodynamic and magneto-hydrodynamic problems; see, e.g. Rogallo (1981), Schumann (1985), Gerz, Schumann & Elgobashi (1989), Kaltenbach, Gerz & Schumann (1994), Brandenburg *et al.* (1995), Hawley, Gammie & Balbus (1995) and Pumir (1996). More recently, Riols *et al.* (2013) found unstable time-periodic solutions embedded in the magneto-hydrodynamic shearing box turbulence by applying Newton's method. Some years later, Sekimoto & Jiménez (2017) found time-periodic solutions for the purely hydrodynamic counterpart using a large-eddy simulation model.

In the second step of H18, the mean state is again locally a constant shear flow but at larger scale its amplitude is assumed to be a slowly varying function of depth. This slowly varying amplitude generates a mean state which is no longer a linear function of distance from the wall and, moreover, is fixed by the global interaction rather than being specified in advance. That situation is reminiscent of the Hall & Lakin (1988) description

of large-amplitude Görtler vortices in boundary layers where it was found that the mean state is that flow which enables the vortex distribution to remain in local neutral stability. Going back further the situation is not unlike that postulated by Malkus (1956) in his marginal theory of turbulence or the suggestion by Benney & Chow (1989) that mean flows might be supported by interacting wave systems. On the other hand, there are many studies concerning the generation of perturbations for given mean states. Linear amplification of wave-like perturbations has been frequently studied in the numerical community (see, e.g. Jiménez 2013), while McKeon & Sharma (2010) studied the associated linear operator using singular value decomposition. In a similar spirit, but focusing more on a local part of the mean flow, the structure and spectra of perturbations generated in the logarithmic layer have long been compared with the shearing box results; see, e.g. Rogers & Moin (1987), Kida & Tanaka (1994) and Sekimoto, Dong & Jiménez (2016). The main point to note here is that, unlike the many phenomenological works where the mean unperturbed state is specified, H18 and the present work deal with a strongly nonlinear interaction in which there is an interplay between the mean and roll–streak–wave flow.

The results of H18 suggested that slowly varying VWI arrays might be a possible mechanism to sustain the universal structure of near-wall turbulent flows. In particular, mean flows with logarithmic profiles might be sustained by arrays of VWI states but the total self-similarity believed to be present within the logarithmic layer could not be predicted. Within the H18 formulation the local array properties must vary with distance from the wall and the 'slow' equation enabling that variation was found to be the mean flow equation of the Reynolds-averaged Navier–Stokes (RANS) equations but with an explicit closure in terms of the local roll and streak parts of the flow. In the present work we will further develop the work of H18 and uncover a second slow evolution equation. The relationship of the new equation to turbulence models such as those of a mixing-length or eddy-viscosity type is not as yet clear. However, the associated constraints imply an alternative interpretation of the properties of the first evolution equation and allow us to judge if self-similarity of coherent structures is possible within the logarithmic layer.

A major difference of the present paper from previous VWI/SSP papers is that our focus is on consistency of equilibrium coherent structures that are generic to the Navier–Stokes equations written in terms of wall units as the distance from the wall increases. We aim to uncover some generic structures of possible widespread relevance motivated by the well-known universal behaviours found in turbulent shear flows. In particular, our main result that the logarithmic law arises only when the coherent structures are localised in the spanwise direction is potentially important. However, we must bear in mind that any structures uncovered when applied to a particular configuration need to be suitably accommodated to the overall flow by rigorous asymptotic matching. The range of validity of our theory could be found when it is applied to particular geometries, but that is not the purpose of the present paper. Therefore, we make no claims about the origin of the logarithmic law for particular flow configurations.

In § 2 we will formulate and solve the periodic VWI array for the homogeneous shear problem and show how they relate to the periodic shearing box approach. In § 3 we will describe several new computational results for VWI periodic arrays in the homogeneous shear flow. This extends the limited numerical results given in H18 for relatively simple states with flat critical layers associated with mirror symmetry. Importantly, the VWI solutions found in this section constitute the leading-order solution of the more general problem described in § 4, where we will reformulate the distributed VWI array problem in wall-layer variables. The basic scales and interactions remain the same as in H18 but we now find two slow evolution equations governing the overall variation of the flow in

the vertical direction. In the same section we will also discuss a possible relationship between particular types of distributed VWI arrays and the attached eddy hypothesis due to Townsend (1951). Finally, in § 5 we will draw some conclusions.

2. Formulation of the VWI array problem in an infinite homogeneous shear flow

In this section we develop the details involved with the description of the VWI array problem, including its connection to the periodic shearing box model previously used by others (see § 1) in simulations of infinite homogeneous shear flows. Consider the non-dimensional incompressible Navier–Stokes equations

$$\partial_t \boldsymbol{u} + \boldsymbol{u} \cdot \boldsymbol{\nabla} \boldsymbol{u} = -\boldsymbol{\nabla} p + Re^{-1} \nabla^2 \boldsymbol{u}, \quad \text{with } \boldsymbol{\nabla} \cdot \boldsymbol{u} = 0, \tag{2.1}$$

where $\boldsymbol{u} = (u, v, w)$ is the velocity, p is the pressure normalized by density and Re is the Reynolds number. In the absence of any nonlinear interaction, we assume that the basic state is the infinite homogeneous shear flow $\boldsymbol{u} = \boldsymbol{u}_b \equiv (y, 0, 0)$, where y is in the normal, or vertical, coordinate direction. The use of shear-periodic boundary conditions implies that the maximum length scale is specified and, hence, statistically steady turbulence can be reached (see Pumir 1996).

The VWI problem for periodic arrays given in H18 can be derived by taking the large-Reynolds-number limit of the shearing box problem, as will be clarified in § 2.1. The presence of the critical layer type theory means that the numerical analysis of the asymptotic problem is however a challenging task, because it requires us to solve singular partial differential equations. Thus, in § 2.2 we describe our strategy to find the numerical approximation of the canonical VWI array solutions; the method is based on the hybrid solution methodology used in Blackburn *et al.* (2013), where it was applied to plane Couette flow. As we shall see in § 4, the generalization of the asymptotic theory using the multiple-scale analysis leads us to include the large-scale variation of the mean flow. The important point to note here is that even when more general mean flows are considered, the same canonical VWI asymptotic problem appears at each local position.

Prior to the asymptotic analysis, here we summarise the properties of the shearing box problem. The shear-periodic boundary conditions used in the problem mean that the flow is not influenced by solid boundaries in the vertical direction. The entire flow is assumed to be made up of cells of constant depth in the y direction superimposed on an infinite constant shear base velocity profile. In a given cell the flow is taken to be identical to that in the cell immediately below/above, except that it propagates in x with a speed equal to the difference in the base flow between adjacent cells. Assuming this shear-periodic condition in y and the usual periodicity in x, z with the wavenumbers $\alpha^\dagger$, $\beta^\dagger$, respectively, the perturbation flow $\boldsymbol{u} - \boldsymbol{u}_b$ satisfies

$$[\boldsymbol{u} - \boldsymbol{u}_b, p](x, y, z, t) = [\boldsymbol{u} - \boldsymbol{u}_b, p]\left(x - nt + l_1 \frac{2\pi}{\alpha^\dagger}, y - n, z + l_2 \frac{2\pi}{\beta^\dagger}, t\right) \tag{2.2}$$

for any integers l_1, l_2, n. Here we have taken the depth of the cell in the y direction as the length scale on which the equations have been made non-dimensional. Hence, l_1 serves as an index on periodicity of fluctuations with respect to the background shear flow $\boldsymbol{u}_b$ in the streamwise x coordinate, l_2 is an index on periodicity in the spanwise z coordinate, while n is an index on periodic repetition (which may include but is not restricted to wavelike periodicity) in the vertical y coordinate. The above conditions imply that, for example, the

pressure can be expressed in the form

$$p(x, y, z, t) = \sum_{m_1} \sum_{m_2} \hat{p}_{m_1 m_2}(y, t)\, \mathrm{e}^{\mathrm{i}(m_1 \alpha^\dagger x + m_2 \beta^\dagger z)}, \tag{2.3}$$

where m_1, m_2 are integers and each sum ranges over $[-\infty, \infty]$. From the condition (2.2), the Fourier coefficients must satisfy

$$\hat{p}_{m_1 m_2}(y, t) = \hat{p}_{m_1 m_2}(y - n, t)\, \mathrm{e}^{-\mathrm{i} m_1 n \alpha^\dagger t} \tag{2.4}$$

for any integer n. This rule must be satisfied by any scalar perturbation quantity.

Unlike parallel wall-bounded problems such as plane Couette or Poiseuille flow, the periodic shearing box problem applied directly to (2.1) does not support simple steady or travelling wave solutions (unless the flow is independent of x); see Riols *et al.* (2013) and Sekimoto & Jiménez (2017). The reason for this is that the shear-periodic boundary condition depends on x and t in a manner which is incompatible with the travelling wave form. However, the asymptotic analysis in the next section shows that some solutions may approach travelling wave states with increasing Reynolds numbers.

2.1. *Large-Reynolds-number asymptotic analysis*

Vortex-wave interaction theory describes the high-Re asymptotic nature of typical coherent structures in shear flows. The leading-order part of the theory naturally shows that the nonlinear interaction between two constituents of flows; the streamwise average flow (i.e. roll–streak field) and a streamwise-oscillatory wave which in streamwise Fourier space is represented by a complex-conjugate pair of monochromatic modes. In Hall & Sherwin (2010) plane Couette flow bounded in the normal (vertical, y) direction by counter-translating walls was considered in order to compare the asymptotic VWI approach with the finite-Reynolds-number results of Wang *et al.* (2007). The VWI array theory of H18 removes the imposition of walls in the normal direction and replaces this with additional periodicity of both the roll and the streak, the latter becoming a periodic variation on a background linear shear flow. The wave is no longer required to be periodic in y but instead is replaced with a periodic array of waves each allowed to be of large vertical extent, a relaxation allowed by the asymptotic structure of this flow constituent, whose interaction with the streamwise average flow is only significant in the critical layer of each wave.

Below we write down the VWI expansions and the interaction equations describing a periodic array of VWI states of unit wavelength in the y direction. The basic scalings for this type of roll–streak–wave interaction remain those introduced by Hall & Smith (1991) and first used in the high-Reynolds-number asymptotic description of numerically exact Navier–Stokes solutions by Hall & Sherwin (2010). For later convenience, we define $(X, Z) = (\alpha^\dagger x, \beta^\dagger z)$. In these new coordinates, the streamwise and spanwise periodic box dimensions are normalised to be 2π. In most parts of the flow, the velocity and pressure expansions of the periodic VWI array found in H18 are

$$u = y + U(y, Z) + \rho \frac{\mathrm{e}^{\mathrm{i}X}}{Re^{7/6}} \sum_{n=-\infty}^{\infty} \mathrm{e}^{-\mathrm{i}\alpha^\dagger n t} \tilde{u}(y - n, Z) + \text{c.c.} + \cdots, \tag{2.5a}$$

$$v = \frac{V(y, Z)}{Re} + \rho \frac{\mathrm{e}^{\mathrm{i}X}}{Re^{7/6}} \sum_{n=-\infty}^{\infty} \mathrm{e}^{-\mathrm{i}\alpha^\dagger n t} \tilde{v}(y - n, Z) + \text{c.c.} + \cdots, \tag{2.5b}$$

$$w = \frac{W(y,Z)}{Re} + \rho\frac{\mathrm{e}^{\mathrm{i}X}}{Re^{7/6}}\sum_{n=-\infty}^{\infty}\mathrm{e}^{-\mathrm{i}\alpha^{\dagger}nt}\tilde{w}(y-n,Z) + \text{c.c.} + \cdots, \tag{2.5c}$$

$$p = \frac{P(y,Z)}{Re^{2}} + \rho\frac{\mathrm{e}^{\mathrm{i}X}}{Re^{7/6}}\sum_{n=-\infty}^{\infty}\mathrm{e}^{-\mathrm{i}\alpha^{\dagger}nt}\tilde{p}(y-n,Z) + \text{c.c.} + \cdots, \tag{2.5d}$$

where c.c. stands for complex conjugate. The two-dimensional complex functions $\tilde{u}, \tilde{v}, \tilde{w}, \tilde{p}$ are referred to as the wave part, while the roll–streak part U, V, W, P are two-dimensional real functions. The ellipses $\cdots$ represent higher-order terms including higher harmonics of the wave. The real constant ρ is the amplitude of the wave. The streak U makes an $O(1)$ modulation to the mean flow so that it generates three-dimensional waves via the inviscid Rayleigh instability mechanism. The $1/Re$ prefactor of vertical–spanwise roll velocity (V, W) is chosen to ensure the viscous-convective balance in the streamwise-averaged flow, noting that only the roll velocity contributes in the convective effect. The boundary conditions to be imposed on the roll–streak flow are periodicity in y, Z so that

$$\boldsymbol{U}(y+1,Z) = \boldsymbol{U}(y,Z+2\pi) = \boldsymbol{U}(y,Z), \tag{2.6a}$$

$$P(y+1,Z) = P(y,Z+2\pi) = P(y,Z). \tag{2.6b}$$

The three-dimensional/three-component wave velocity field in (2.5) is, in the majority of the domain, smaller than that of the roll by a factor $Re^{1/6}$ and, thus, at first glance does not cause any feedback effect to the leading-order roll–streak. However, the wave becomes stronger within the thin critical layer of thickness $O(Re^{-1/3})$, where the feedback effect occurs (the amplification can be seen in figures 2 and 3). The scaling of the wave is chosen in order that the Reynolds stresses in the critical layer produced by the wave drive the roll flow; see Hall & Sherwin (2010) for a more detailed discussion of the scaling. The summations in (2.5) represent contributions from the infinite vertical array of waves. Individual waves are periodic in the streamwise and spanwise directions, and repetitive, but not assumed periodic in the vertical direction. As described in H18, the magnitude of each wave component takes on its maximum values within its associated critical layer and then decays to zero exponentially in neighbouring cells. For example, the wave pressure satisfies

$$\tilde{p}(y,Z) = \tilde{p}(y,Z+2\pi), \tag{2.6c}$$

$$\tilde{p}(y,Z) \to 0, \ \ y \to \pm\infty. \tag{2.6d}$$

Although an individual wave is not periodic in y, the entire superimposed array of the roll–streak–waves (2.5) does satisfy the spectral form of the shear-periodic conditions (2.4).

The factors $\mathrm{e}^{-\mathrm{i}\alpha^{\dagger}nt}$ in the summation account for the fact that the speeds of waves centred in vertically neighbouring cells differ by unity to match the change in mean flow speed between adjacent cells. We note that in the expansions above one could replace nt in the exponential terms by $(n+c)t$ in order to describe the situation where each wave propagates at a phase speed c different from the unperturbed flow speed at the centre of each cell. Here we describe the case where all the waves have an identical structure so that we could also then shift the origin in y to reduce c to zero, thereby recovering (2.5). However, a more detailed consideration of the phase speed would be essential in cases where waves of distinct properties participate in the array. For example, in § 3.2 we

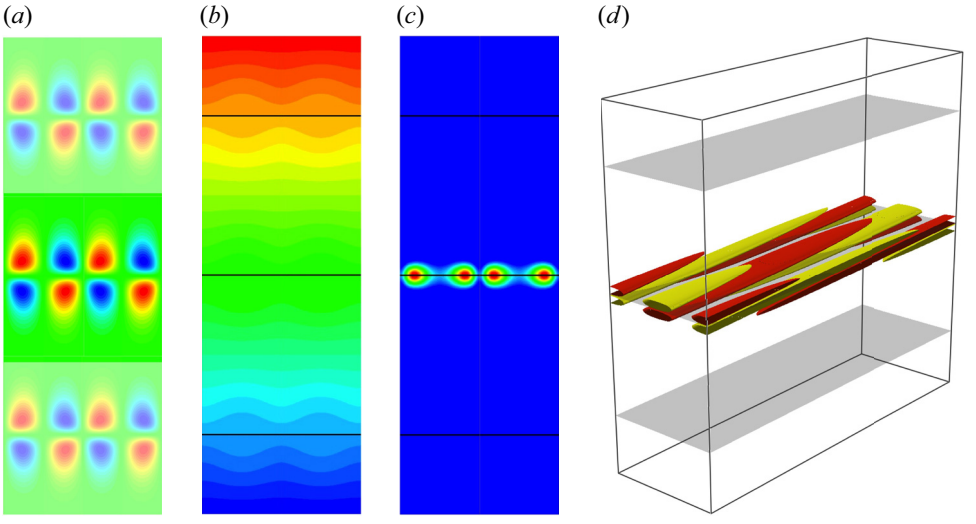

Figure 2. Solution for the mirror-symmetric mode at $\alpha^\dagger = 2$, $\beta^\dagger = 2\pi$, $R_f = 20 \times 10^3$. Horizontal axis is z, vertical axis is y. The domain shown is $y \in [-5/2, 5/2]$, $z \in [0, 2\pi/\beta^\dagger]$. (*a*) Contours of roll stream function ψ in the (y, z) plane shown for three fundamental vertical modules. A slightly lightened colour is used except for the central module $y \in [-1/2, 1/2]$. (*b*) Contours of streak flow $y + U$ on the domain used to solve for the wave $\tilde{\boldsymbol{u}}$. Critical layers for waves with speeds $0, \pm 1$ are shown as black lines. (*c*) Contours of kinetic energy $|\tilde{\boldsymbol{u}}|^2$ for the central stationary wave. (*d*) Three-dimensional structure of $\tilde{\boldsymbol{u}}$ for the central stationary wave shown as red/yellow isosurfaces of positive/negative streamwise vorticity. The critical layers for the waves with speeds $0, \pm 1$ are shown as translucent planes.

treat the flow maintained by two waves that move in opposite directions. In that case the c-dependence would need to be retained and we would split the summations in (2.5) into two sums representing the two sets of waves.

Substituting the expansions (2.5) into (2.1), we can find a leading-order system valid outside of the critical layer. As anticipated, the streamwise-invariant roll–streak part satisfies advection-diffusion equations

$$V + VU_y + \beta^\dagger WU_Z = U_{yy} + \beta^{\dagger 2} U_{ZZ}, \tag{2.7a}$$

$$VV_y + \beta^\dagger WV_Z = -P_y + V_{yy} + \beta^{\dagger 2} V_{ZZ}, \tag{2.7b}$$

$$VW_y + \beta^\dagger WW_Z = -\beta^\dagger P_Z + W_{yy} + \beta^{\dagger 2} W_{ZZ}, \tag{2.7c}$$

$$V_y + \beta^\dagger W_Z = 0. \tag{2.7d}$$

The wave part satisfies the inviscid instability problem for the base flow $y + U(y, Z)$, which after some manipulation becomes the single equation for the wave pressure function $\tilde{p}$,

$$\left(\frac{\tilde{p}_y}{\{y + U(y, Z)\}^2}\right)_y + \left(\frac{\beta^{\dagger 2}\tilde{p}_Z}{\{y + U(y, Z)\}^2}\right)_Z - \frac{\alpha^{\dagger 2}\tilde{p}}{\{y + U(y, Z)\}^2} = 0. \tag{2.7e}$$

Given the base flow $y + U(y, Z)$, the wave equations constitute a linear eigenvalue problem. The wave pressure function $\tilde{p}(y, Z)$ is normalised such that the integral of $|\tilde{p}|^2$ over the streamwise-normal area of the periodic box is unity. In order to find the size of

the wave measured by the amplitude ρ we consider the feedback effect of the wave to the roll–streak.

The periodic roll–streak flow is supported by a periodic array of waves each of which interacts only significantly in the critical layer. The amplification mechanism of the wave there is due to the singularity of (2.7*e*) occurring when $y + U(y, Z)$ vanishes. The classical critical layer argument can be used to show that within a thin layer of thickness $O(Re^{-1/3})$ surrounding the singularity, one must alter the form of the asymptotic expansions. The viscous effect in the wave equations is no longer negligible there, and singularity observed in the outer scale is regularised in the inner scale. Remarkably, an analytical solution exists for the critical layer problem, and we can write the feedback effect down explicitly in terms of the jump of the roll–streak quantity across the critical layer. The jump conditions are most easily expressed in terms of V^s, the component of the roll flow locally parallel to the critical layer, using the new variables s, N which measures distance along and normal to the layer in the (y, z) coordinate. From Hall & Smith (1991) and Hall & Sherwin (2010), the jumps are found to be

$$\left[\frac{\partial V^s}{\partial N}\right]_-^+ = J'(s), \quad [P]_-^+ = -\chi(s)J(s), \tag{2.8a,b}$$

where $\chi(s)$ is the curvature of the critical layer and

$$J(s) = \left.\frac{n_0\rho^2|\tilde{p}_s|^2}{\{\alpha^\dagger(y+U)_N\}^{5/3}}\right|_{N=0}, \quad n_0 = 2\pi\left(\frac{2}{3}\right)^{\frac{2}{3}}\left(-\frac{2}{3}\right)!. \tag{2.9a,b}$$

If the critical layer is flat the above jumps reduce to

$$\left[\frac{\partial W}{\partial N}\right]_-^+ = \beta^\dagger\hat{J}'(Z), \quad [P]_-^+ = 0, \quad \hat{J}(Z) = \left.\frac{n_0\rho^2\beta^{\dagger 2}|\tilde{p}_Z|^2}{\{\alpha^\dagger(1+U_y)\}^{5/3}}\right|_{N=0}, \tag{2.10a–c}$$

as used in H18. Once again we note that if there is more than a single critical layer in each cell, one must compute the jumps across each layer induced by the relevant wave.

The equations (2.7), the boundary conditions (2.6), the jump conditions (2.8*a*,*b*) and the wave pressure normalisation constitute a closed nonlinear eigenvalue problem. The solution of that canonical problem for given $\alpha^\dagger$, $\beta^\dagger$ determines the leading-order structure $(\boldsymbol{U}, \tilde{p})$ in the leading-order part of the expansion (2.5), together with the amplitude $\rho(\alpha^\dagger, \beta^\dagger)$.

In the high-Reynolds-number limit any neutral wave travelling in the flow will reinforce locally a flow in the y–z plane predominantly by producing a stress jump associated with its own critical layer. The overall structure of the single wave interaction problem is unchanged from the usual VWI for parallel flows. This is advantageous for computations because the numerical solution of the canonical problem can be found using existing VWI codes for travelling wave solutions in plane Couette flow with some minor modifications (see § 2.2, following).

As remarked earlier, the boundary conditions used for the canonical problem are consistent with the shear-periodic conditions. This means that some time-periodic solutions of the finite-Reynolds-number shearing box problem as found, for example, by Sekimoto & Jiménez (2017) might asymptote to the VWI structure described by the canonical problem even though the asymptotic solution is of travelling wave form. On first consideration, this might seem a rather paradoxical outcome. However, we recall that the travelling wave form of the leading-order structure is possible because in the asymptotic framework the fundamental mode is induced by the linear stability problem

of the streak field. Thus, the interaction of fundamental waves centred in different cells induces higher streamwise harmonics of a non-travelling wave form in (2.5), and formally they are smaller than the fundamental mode. This means that an intrinsic property of periodic box solutions – that no pure travelling wave states are possible – is actually a finite-Reynolds-number effect.

A referee of this work has kindly pointed out similarities of H18 and the present paper to Montemuro *et al.* (2020). The latter was a development of an earlier paper, Chini *et al.* (2017), with significant modifications to the streamwise wavelength scales. The essential structure proposed in those papers is closely related to H18. However, the roll activity is taken to be sufficiently large that the streamwise velocity becomes uniform and the critical layer driving the interaction becomes embedded in an outer layer where the streamwise velocity adjusts between its different constant values in adjacent cells. In previous VWI and SSP problems it has been found that for a given periodic box size all flow quantities are determined by solving a nonlinear eigenvalue problem, while Montemuro *et al.* (2020) found that for a given periodic box size solutions exist for a continuum of values of the wave amplitude. This apparently surprising result perhaps arises because the streak profile in the new layer surrounding the critical layer becomes independent of the wave amplitude and roll driven by the wave. One might anticipate that similar structures could be found numerically from the hybrid formulation below but exhaustive searches did not find any such solutions.

2.2. *Hybrid approach*

As remarked earlier, the VWI formulation of H18 reduces the Navier–Stokes equations to a coupled pair of two- rather than three-dimensional momentum equations and takes the Reynolds number out of the problem. Nevertheless, the computational treatment of the asymptotically reduced problem (2.6)–(2.8*a*,*b*) is challenging because of the stress jump conditions to be applied across the wave's critical layer, whose position is *a priori* unknown. Here we adopt the 'hybrid' methodology first advanced in Blackburn *et al.* (2013) and used subsequently by Deguchi & Hall (2016). The key aspect of the methodology is to regularise the critical layer singularity by retaining some viscous effects in the reduced system, allowing us to use with only minor variations conventional numerical methods developed for solution of Navier–Stokes problems. The strength of the regularisation is measured by the 'fictitious Reynolds number' R_f, here based on the depth of the fundamental vertical module and the background shear, and as in Blackburn *et al.* (2013), we check that outcomes become independent of this parameter as it increases.

Here we remark that the reduced Navier–Stokes computations employed later by Thomas *et al.* (2014) and Beaume *et al.* (2015, 2016) are essentially equivalent to the hybrid approach. All these methods rely on solving the finite-Reynolds-number Navier–Stokes equations reduced to just two streamwise Fourier modes: the streamwise average (the 'vortex', or roll–streak) and a single streamwise wave. The hybrid equations can be obtained by further assuming that there is no wave Reynolds stress driving the streak (U), and that the roll components (V, W) can be neglected in the wave equations. Both assumptions follow from the fact that the roll velocity is much smaller than that of the streak (see (2.5)). All reductions make explicit recognition of the crucial tripartite interaction between rolls, streaks and waves in the VWI theory.

Starting the hybrid reduction process from the Navier–Stokes equations (2.1) with the leading-order part of the VWI expansions shown in (2.5), and setting $Re = R_f$, we get the

roll–streak equations from the x-averaged part

$$(V\partial_y + \beta^\dagger W\partial_Z)\begin{bmatrix} y+U \\ V \\ W \end{bmatrix} = -\begin{bmatrix} 0 \\ \partial_y P \\ \beta^\dagger \partial_Z P \end{bmatrix} + (\partial_{yy} + \beta^{\dagger 2}\partial_{ZZ})\begin{bmatrix} U \\ V \\ W \end{bmatrix} - R_f^{-1/3}\rho^2 \sum_{n=-N}^{N} \begin{bmatrix} 0 \\ F_1^{(n)} \\ F_2^{(n)} \end{bmatrix}, \tag{2.11}$$

which, note, are solved at a unit effective Reynolds number owing to the adoption of the asymptotic scaling (Hall & Smith 1991; Hall & Sherwin 2010), while the x-fluctuation part yields the wave equations

$$\mathrm{i}\alpha^\dagger(y+U-c)\begin{bmatrix} \tilde{u} \\ \tilde{v} \\ \tilde{w} \end{bmatrix} + \begin{bmatrix} \tilde{v}\partial_y(y+U) + \beta^\dagger \tilde{w}\partial_Z U \\ 0 \\ 0 \end{bmatrix} = -\begin{bmatrix} \mathrm{i}\alpha^\dagger \tilde{p} \\ \partial_y \tilde{p} \\ \beta^\dagger \partial_Z \tilde{p} \end{bmatrix} + R_f^{-1}\nabla^2 \begin{bmatrix} \tilde{u} \\ \tilde{v} \\ \tilde{w} \end{bmatrix}. \tag{2.12}$$

Owing to the presence of the viscous term, (2.12) are not singular. We have here allowed for a non-zero wave speed c, allowing us to obtain the type of results to be described in § 3.2 below, though, as discussed in § 2.1, we could equally well have used a slight elaboration to the form of (2.5) (where $c = 0$). The final terms in (2.11) represent the Reynolds stresses from the waves

$$F_1^{(n)} = \partial_y\{\tilde{v}(y-n,Z)\tilde{v}^*(y-n,Z)\} + \beta^\dagger\partial_Z\{\tilde{v}(y-n,Z)\tilde{w}^*(y-n,Z)\} + \text{c.c.},$$
$$F_2^{(n)} = \partial_y\{\tilde{v}(y-n,Z)\tilde{w}^*(y-n,Z)\} + \beta^\dagger\partial_Z\{\tilde{w}(y-n,Z)\tilde{w}^*(y-n,Z)\} + \text{c.c.},$$

where $*$ denotes complex conjugation and N should formally be taken to be large in order to recover an infinite array system. These stress terms are inserted in body force form because, owing to the viscous term in the wave equations, the thickness of the critical layer becomes finite. Note that these body force terms were absent in the formal asymptotic reduction (2.7) since the stress terms at the asymptotic limit are concentrated within the infinitely thin critical layer and, hence, become discontinuous stress jumps across the layer as given in (2.8*a*,*b*).

Now consider the fundamental vertical cell $y \in [-1/2, 1/2]$ for the numerical computations. We enforce periodic conditions of period unity for the roll–streak. In general, the Reynolds stress term from waves in cells above and below the module must be accounted for. However, for many of the numerical solutions which follow, the critical layer is trapped within the fundamental module. In that case we can set $N = 0$ such that each roll is influenced only by the wave inside its local module, since the stress is significant only around the critical layer (it is possible to relax this restriction if required). Each wave decays exponentially with increasing distance from its corresponding module. For the wave component, it is typically sufficient to consider a domain of depth three to five units with no-slip or no-stress conditions imposed at its upper and lower edges.

The preceding discussion assumes that all waves have an identical structure. Next we consider the case when two distinct waves coexist in one period of the roll–streak flow. In order to compute this second mode, we exploit the property that the two waves possess certain symmetries, allowing us to compute over only half of the periodic structure, and,

hence, it is convenient to choose the depth of the fundamental module to be half of the roll–streak period, such that it encloses only one wave critical layer.

We solve the hybrid system numerically at finite but large enough R_f, checking that the solution is in the asymptotic range where the wave amplitude ρ required to produce an equilibrium state becomes independent of R_f. We have employed two alternative, and equivalent, means to finding solutions to the system ((2.11), (2.12)). The first method couples a large-time τ-integration of the unsteady version of (2.11) (i.e. $\partial_\tau [U, V, W]^{\mathrm{T}}$ is added in the left-hand side) with the eigenvalue analysis of (2.12), using spectral elements to discretise both equations. The former time integration problem can be solved if the wave forcing is given, and the latter eigenvalue problem returns the complex phase speed c for a given streak field. The wave amplitude ρ is tuned to neutralise the growth rate of the wave in a relaxation iteration based on the successive updates of the wave and roll–streak fields until reaching a fixed point; this was the approach adopted in Blackburn *et al.* (2013). The convergence of a time-stepper-based eigensolution method used in the scheme depends on the stability of the solution. For lower-branch solutions, the neutrally stable Rayleigh mode is the least stable one and there is no difficulty in obtaining convergence. However, for upper-branch solutions, unstable Rayleigh modes typically exist in addition to a neutrally stable one (Gibson, Halcrow & Cvitanović 2009; Deguchi & Hall 2016), and, hence, a shift-invert solution method outlined in Gómez *et al.* (2015) is used to isolate neutrally stable modes. Using this slight modification to our original methodology we were here able to find both upper- and lower-branch solutions with the fixed-point technique, something which did not prove possible in the earlier work, which contained only lower-branch solutions. The second method uses Chebyshev–Fourier/Fourier–Fourier global expansions for discretising the waves/roll–streaks and directly solves the resultant algebraic equations by the Newton–Raphson method. The Navier–Stokes solver developed in Deguchi, Hall & Walton (2013) can be modified to find solutions of ((2.11), (2.12)); this was the approach adopted in, for example, Deguchi & Hall (2016). The fixed-point iteration code is useful in finding solutions from fairly arbitrary initial conditions, while the Newton–Raphson code provides an efficient continuation method to trace the solution branch without regarding its stability. We confirmed that the two methods produce the same outcomes at matching values of $\alpha^\dagger, \beta^\dagger, R_f$.

3. Numerical results for the canonical VWI array problem

A central tenet of the VWI array solutions we seek is that the roll–streak solution is periodic in the cross-flow directions, sustained by an infinite periodic array of waves which individually are of larger cross-flow extent, but which are of dominant dynamic significance only for each associated roll. These features will become apparent in the solutions shown below. As in H18, the present solutions assume that waves are periodic in the spanwise direction on the same length scale as the roll–streak flow, but are of 'infinite' vertical extent in the vertical direction. In order to treat the solutions numerically, we approximate the domains for the wave components by adopting computational boxes for those components which are much larger in y-extent than the roll–streak vertical module length. Note that outcomes in this section are presented in terms of unmapped coordinates (x, y, z). Recall that the fundamental module is defined as $(x, y, z) \in [0, 2\pi/\alpha^\dagger] \times [-1/2, 1/2] \times [0, 2\pi/\beta^\dagger]$.

3.1. *Mirror-symmetric and sinuous modes*

The numerical results presented here were motivated by the previous findings of two typical steady solutions in plane Couette flow. The first is the mirror-symmetric mode

found by Itano & Generalis (2009) and Gibson *et al.* (2009) where in the latter, the labels EQ7 and EQ8 were used. This mode has some similarity to the VWI array solution found in H18. The second is the sinuous-mode solution found by Nagata (1990), Clever & Busse (1992) and Waleffe (1998) and labelled EQ1 and EQ2 in Gibson *et al.* (2009). This mode has been the most intensively studied among other numerous solutions, because it is the first to appear when the Reynolds number is increased, and the lower branch created by that saddle-node bifurcation defines the edge of the laminar and turbulent attractors (Wang *et al.* 2007). The large-Reynolds-number asymptotic development of the branch has been explained by applying the VWI theory to that branch (Hall & Sherwin 2010; Blackburn *et al.* 2013; Deguchi & Hall 2014*b*, 2016). The sinuous mode possesses so-called shift-reflection and shift-rotation symmetries

$$[u, v, w](x, y, z) = [u, v, -w](x + \pi/\alpha^{\dagger}, y, -z), \tag{3.1a}$$

$$[u, v, w](x, y, z) = [-u, -v, w](-x, -y, z + \pi/\beta^{\dagger}), \tag{3.1b}$$

while the mirror-symmetric mode satisfies those two symmetries and

$$[u, v, w](x, y, z) = [-u, -v, w](-x + \pi/\alpha^{\dagger}, -y, z). \tag{3.1c}$$

Indeed, Deguchi & Hall (2014*a*) found a bifurcation point at which the sinuous-mode branch bifurcates from the mirror-symmetric mode branch by a symmetry breaking of (3.1*c*).

Here we consider how those symmetries could be carried over to our triply periodic problem. It is convenient to begin by first demonstrating that the mirror symmetry (3.1) imposed for the roll–streak field can reproduce features of the VWI array solutions presented in H18. The roll–streak field version of (3.1) can be found as

$$[U, V, W](y, z) = [U, V, -W](y, -z), \tag{3.2a}$$

$$[U, V, W](y, z) = [-U, -V, W](-y, z + \pi/\beta^{\dagger}), \tag{3.2b}$$

$$[U, V, W](y, z) = [-U, -V, W](-y, z). \tag{3.2c}$$

From the third condition we see that $U = 0$ at $y = 0$. Such a flat critical layer is special in the sense that the wave pressure admits a regular expansion there and, hence, presents less numerical difficulty (see Deguchi & Hall 2016, H18 and Deguchi 2019). In fact, the numerical technique used by H18 can be applied only for this case. As we shall see shortly, for the sinuous mode, the critical layer is curved, owing to the absence of the symmetry (3.2*c*), and, hence, in order to resolve the singular critical layer structure the hybrid method must be employed.

Imposing (3.2) and periodicity in y with unit wavelength for the roll–streak field, we are able to generate the mirror-symmetric mode solution shown in figure 2. In figure 2(*a*), for presentation of roll velocity field (V, W), we use contours of stream function ψ, where $\beta^{\dagger}\partial_Z\psi = -V$ and $\partial_y\psi = W$. Three modules of depth unity are shown; except for the centre module $y \in [-1/2, 1/2]$, the colour map is slightly lightened (and owing to the colour map chosen, variations in streak speed around the central critical layer may be difficult to perceive, but are similar in nature to the more visible variations near the other two critical layers shown). The rolls redistribute the streamwise velocity to create the streaky pattern shown in (*b*), which in turn generates the wave field shown by figure 2(*c*,*d*) via the wave equations (2.12) that are solved on domains of large but finite vertical extent. We note that within the domain shown in figure 2(*c*), three critical layers for waves of speeds 0, ± 1 may coexist, as shown by the black lines. Our focus in the computation is on

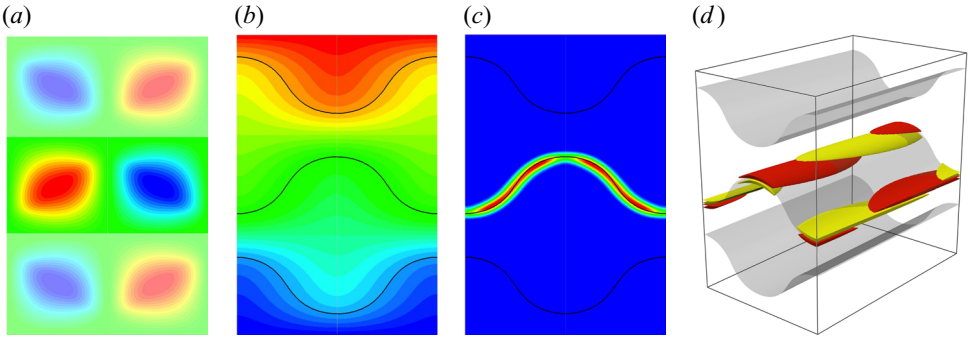

Figure 3. A lower-branch solution for the sinuous mode at $\alpha^\dagger = 2$, $\beta^\dagger = \pi$, $R_f = 20 \times 10^3$. Panels as for figure 2.

resolving the central wave that is both neutral and stationary; the nature of other neutrally stable waves is identical to the centre wave and, hence, are not shown in figure 2(*c*,*d*). The generated centre wave $\tilde{\boldsymbol{u}}$ indeed satisfies the symmetries (3.1). In order to solve (2.12) for the centre wave, here a domain three times greater than the roll–streak module (i.e. $y \in [-3/2, 3/2]$) was used. As may be seen in figure 2(*c*,*d*) each wave localises around its critical layer, and falls rapidly in strength with distance from the layer, consistent with the asymptotic theory. Only one critical layer is present in each roll–streak module and, thus, we can set $N = 0$ in (2.11) to calculate the feedback effect from the waves to the rolls.

Now we turn our attention to the sinuous mode. From the plane Couette flow results we anticipate that a pair of counter-rotating rolls form within a periodic box. If such rolls are generated in the fundamental module, it would be more natural to combine a half-shift in z with the periodic boundary conditions in y, in order to tile the infinite domain. Thus, we impose

$$[U, V, W](y, z) = [U, V, W](y + 1, z + \pi/\beta^\dagger), \tag{3.3}$$

rather than the usual periodicity. A solution generated by imposing symmetries (3.2*a*), (3.2*b*), (3.3) is shown in figure 3. From figure 3(*a*) it is evident that the shift-periodic symmetry (3.3) generates a feature characteristic of sinuous-mode arrays: rolls in vertically and horizontally adjacent cells counter-rotate, chequerboard fashion. In other words, the period of the roll–streak field is twice unity in y rather than unity; thus, except for this minor rescaling for numerical convenience, the structure here is fully covered by the asymptotic theory of § 2. Combining (3.2*b*) and (3.3), we see that the roll–streak (U, V, W) has reflectional symmetry with respect to the edge of the fundamental box. As seen in figure 3(*b*), the critical layers for the waves of speeds ± 1 are placed symmetrically to that for the centre wave. The kinetic energy of the centre wave is trapped within the fundamental module (see figure 3*c*), and, thus, we can use the same numerical technique as adopted for the mirror-symmetric mode, again with $N = 0$. As should be apparent from an examination of figure 3(*d*), the centre wave $\tilde{\boldsymbol{u}}$ satisfies symmetries (3.1*a*) and (3.1*b*).

3.2. *Spatial intermittency*

Interestingly, when a wider domain is used, our periodic array computation is able to capture spanwise-isolated solutions similar to those found in the plane Couette flow by Schneider, Gibson & Burke (2010*a*), Schneider, Marinc & Eckhardt (2010*b*), Deguchi *et al.* (2013) and Gibson & Brand (2014). The solution shown in figure 4 is an example, which may be considered a counterpart of one of the plane Couette flow solutions in Schneider

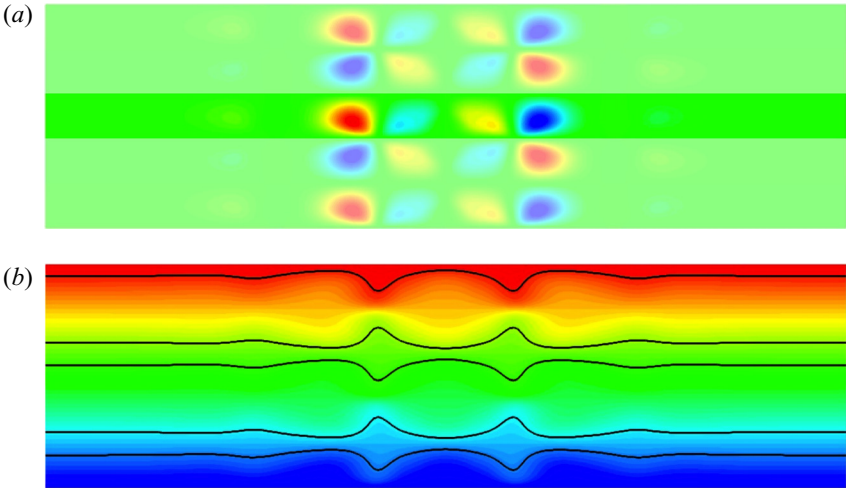

Figure 4. A spanwise-isolated solution at $\alpha^\dagger = 0.8$, $\beta^\dagger = 0.35$, $R_f = 40 \times 10^3$. Domain shown is $y \in [-5/2, 5/2]$, $z \in [0, 2\pi/\beta^\dagger]$. (*a*) Contours of roll stream function ψ. (*b*) Contours of total streak flow $y + U$. Critical layers for waves with speeds $2 + c$, $1 - c$, c, $-1 - c$, $-2 + c$ with $c = -0.24$ are shown as black curves.

et al. (2010*a*,*b*), originating in a symmetry breaking bifurcation of the shift-rotation symmetry (3.1*b*) from the sinuous mode. By analogy, only (3.2*a*) and (3.3) are imposed for the roll–streak to generate the solution shown in figure 4. The structure of each roll cell is similar to that observed in the sinuous mode (see figure 3*a*), but these now only appear in a subinterval of z smaller than the box dimension. The central wave is solved in a domain five times deeper than the fundamental module using the total streak field shown in figure 4(*b*). The wave satisfies (3.1*a*) but not (3.1*b*), and, hence, it is no longer stationary. Nevertheless, the reflectional symmetry with respect to the edge of the modules survives, meaning that the wave in the module adjacent to the central module propagates in the opposite direction with the same absolute speed, if the unit increment of the wave speed is ignored. In figure 4 (*b*) critical layers exist at $U = 2 + c$, $1 - c$, c, $-1 - c$, $-2 + c$, from top to bottom, where $c = -0.24$ is the speed of the most central wave.

It is clear from the flow visualisation of figure 4 that the typical scale of the flow variation in the spanwise direction is comparable to the vertical module, rather than the spanwise dimension of the computational box size. In fact, the perturbation field decays exponentially in large z, and, hence, for sufficiently small $\beta^\dagger$, the coherent structure becomes insensitive to changes of the width of the box. This strongly suggests that there is a limiting solution in the limit of $\beta^\dagger \to 0$. The existence of such a spanwise-isolated canonical array solution is the basis of the discussion in § 4, where the multiple-scale version of the VWI array theory will be used to derive the logarithmic law of the wall.

3.3. *Momentum transport and emergence of uniform momentum zones*

Now let us examine the typical parameter dependence of the solutions drawing the solution branch by varying $\alpha^\dagger$ for fixed $\beta^\dagger$. Here we choose the sinuous mode as the representative solution.

In order to illustrate the bifurcation diagram, we need to select a typical scalar flow quantity. The shear of the mean flow on the wall is commonly used as a measure of nonlinear states in the computational study of wall-bounded shear flows, because it can be

related to the momentum transport. For our triply periodic VWI problem, by integrating the streak (2.7*a*) over one period in Z we can deduce the fact that the momentum transport σ defined by

$$\sigma = \frac{\mathrm{d}U_m}{\mathrm{d}y} - \frac{1}{2\pi}\int_0^{2\pi} UV\,\mathrm{d}Z \tag{3.4}$$

must be a constant for all y. Here we have defined the mean flow distortion by

$$U_m(y) = \frac{1}{2\pi}\int_0^{2\pi} U\,\mathrm{d}Z. \tag{3.5}$$

For the sinuous and mirror-symmetric modes, there are axes of symmetry (e.g. $y = \pm 1/2$) on which V vanishes. Thus, for those modes the momentum transport and the shear of the mean flow are related by $\sigma = (\mathrm{d}U_m/\mathrm{d}y)|_{y=\pm 1/2}$, similar to wall-bounded flows. We also note that by further integrating (3.4) over one period in y we can establish the simple relationship

$$\sigma = -\langle UV\rangle, \tag{3.6}$$

where $\langle\,\rangle$ denotes an average over one periodic box in the y, Z plane. As shown by H18 and to be discussed in § 4, the quantity $\sigma(\alpha^\dagger, \beta^\dagger)$ plays an important role when the VWI array theory for the homogeneous shear flow is extended by the method of multiple scales.

Figure 5 illustrates the variation of σ along the sinuous-mode solution branch. Here we use $\beta^\dagger = 4$, i.e. the same box aspect ratio used to draw the bifurcation diagram of plane Couette flow study in figure 1 of Deguchi & Hall (2014*c*) (hybrid systems for both flows become identical except for boundary conditions). The overall bifurcation diagram of the array problem (solid curve) is similar to that for the plane Couette flow computed in Deguchi & Hall (2014*c*) (dashed curve). The branch turns back around $\alpha^\dagger \approx 2.86$. The existence of the turning point suggests that the flow may have a minimal flow unit, consistent with the observation in finite-Reynolds-number shearing box simulations by Sekimoto *et al.* (2016). According to the empirical observation of that paper, the shearing box turbulence generates typical properties of near-wall turbulence when $\beta^\dagger/\alpha^\dagger \gtrsim 2$ and $\beta^\dagger \gtrsim \pi$. The computational boxes we selected in figure 6(*a*,*b*) satisfy those conditions.

Upon passing the turning point, the upper-branch solutions are harder to resolve in the channel flow studies, and this is indeed the case here. The difficulty is due to the eventual emergence of a homogenised zone developing in the streak field. The upper panels of figure 6 show that the homogenisation develops with decreasing $\alpha^\dagger$, associated with progressively more contorted critical layers. As the lower panels of figure 6 illustrate, when the critical layer straddles the homogenised zone, the local shear around the layer must necessarily be weak, meaning that we need very large R_f in order to ensure the thinness of the critical layer. In figure 5 the asymptotic convergence of the solution was checked by increasing R_f up to 280×10^3. For such very large values of R_f, the critical layer near the non-homogenised zone becomes extremely thin, as seen in figure 6(*a–c*). This multi-scale feature of the flow along the critical layer requires very high resolution in the computation (to resolve the wave structure, here we have employed 640 Chebyshev modes in the vertical direction, while up to 42 Fourier harmonics are considered in Z). These features of the upper-branch solutions are reminiscent of the results of Deguchi & Hall (2014*c*), where uniform momentum zones were found for the first time for equilibrium solutions in plane Couette flow.

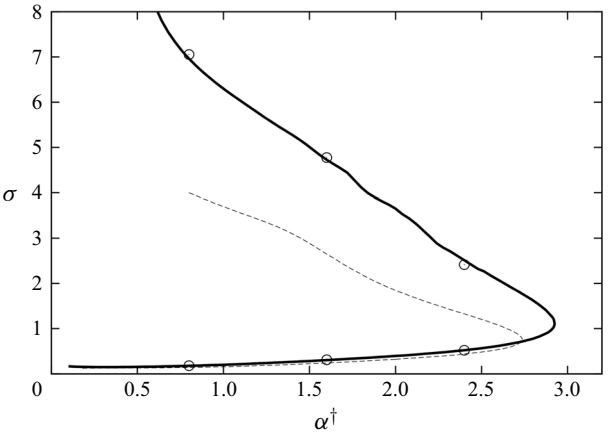

Figure 5. Bifurcation diagram for the sinuous mode at $\beta^\dagger = 4$ showing variation of momentum-transport parameter σ (see text) as a function of streamwise wavenumber $\alpha^\dagger$. Solid line: $R_f = 280 \times 10^3$; open circles: $R_f = 200 \times 10^3$; dashed line: equivalent result for plane Couette flow geometry by Deguchi & Hall (2014*c*).

4. Slowly varying VWI arrays in the wall layer

There is much evidence to suggest that the wall-layer structure shown in figure 1, with the so-called logarithmic layer interposed between the buffer layer and the wake region, is ubiquitous in externally driven high-Reynolds-number turbulent boundary layers. Since Townsend (1951, 1976) hypothesised that the logarithmic layer would be made up of self-similar energy containing motions of size proportional to the distance from the wall, there have been numerous attempts to confirm the hypothesis, as summarised in § 1. Here we investigate whether the attached eddy hypothesis for the logarithmic layer can be exhibited by distributed arrays of VWI interactions.

Since the structure of near-wall turbulent boundary layers is believed by many researchers to be generic to all shear flows, it is natural to start formulation of possible array interactions within the context of the unit-Reynolds-number Navier–Stokes equations appropriate to wall-unit scalings. The effective Reynolds number is then a function of the distance from the wall and, based on numerical simulations, can be taken to be large. We will build on the initial work of H18 on distributed arrays but with the distance from the wall as the large parameter used to separate scales and the components of the self-sustaining motion. In order to see the key points more clearly we focus on modes for which the critical layer is flat; the more general case will lead to similar evolution equations and conclusions but makes their derivation more cumbersome.

Consider a viscous incompressible flow in the half-plane $\hat{y} > 0$ with respect to dimensional Cartesian coordinates $(\hat{x}, \hat{y}, \hat{z})$. If we let $\hat{\tau}_w$ denote the wall shear and $\hat{\rho}$, $\hat{\mu}$ denote the fluid's density and viscosity then we take $\hat{u}_\tau = (\hat{\tau}_w/\hat{\rho})^{1/2}$. The form of the particular flow under consideration will be felt through the conditions to be imposed sufficiently far from the wall. Using $\hat{\mu}/(\hat{\rho}\hat{u}_\tau)$ as the length scale in the problem and $\hat{\mu}/(\hat{\rho}\hat{u}_\tau^2)$ as the time scale, the dimensionless Navier–Stokes equations written with respect to dimensionless variables Cartesian coordinates x, y, z, and time t become

$$\partial_t \boldsymbol{u} + \boldsymbol{u} \cdot \boldsymbol{\nabla} \boldsymbol{u} = -\boldsymbol{\nabla} p + \nabla^2 \boldsymbol{u}, \quad \text{with } \boldsymbol{\nabla} \cdot \boldsymbol{u} = 0, \tag{4.1}$$

where p is the dimensionless pressure. Once again we stress that, if the structure we seek is to universally hold in turbulent shear flows, it must be expressed in wall units.

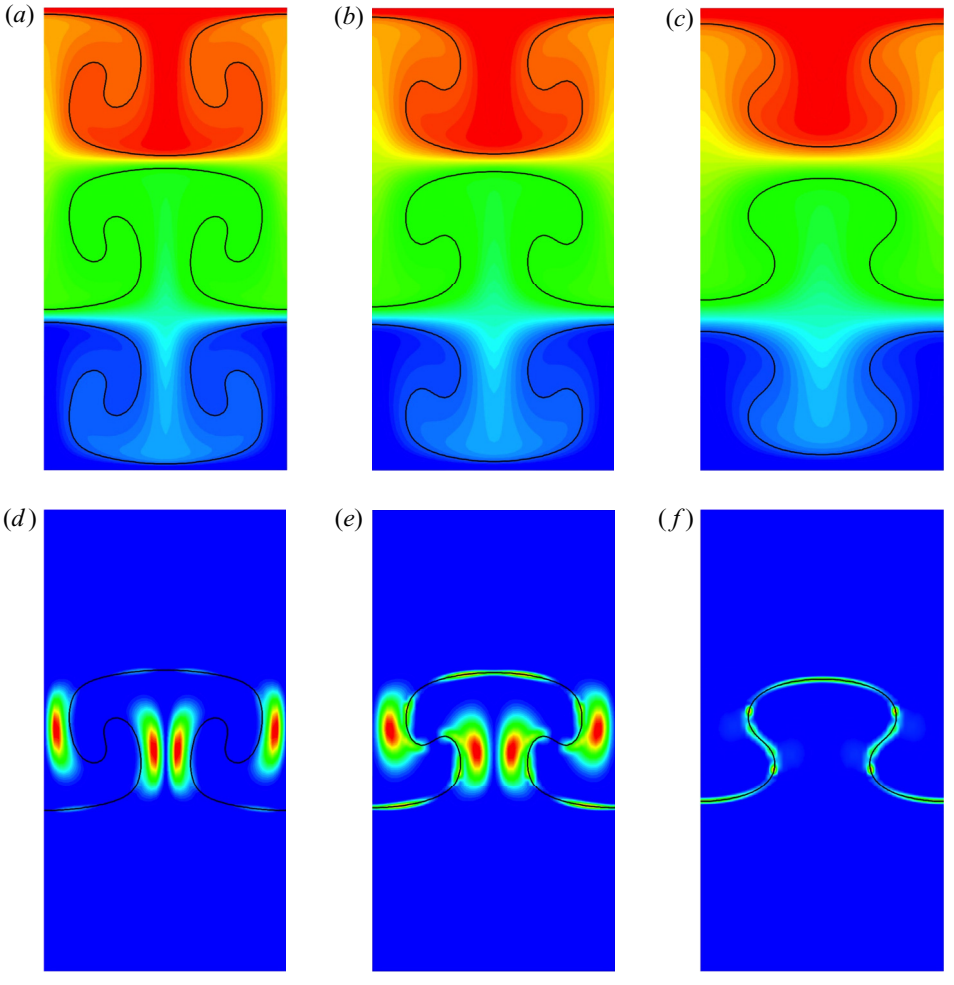

Figure 6. Upper-branch sinuous-mode solutions at $\beta^\dagger = 4$, showing the effect of streamwise wavenumber $\alpha^\dagger$. (*a–c*) Contours of total streak ($y + U$) for $\alpha^\dagger = 0.8$, 1.6, 2.4, respectively, with critical layers for waves with speeds -1, 0, 1. (*d–f*) Corresponding contours of kinetic energy $|\tilde{\boldsymbol{u}}|^2$ for the stationary wave with its critical layer.

When our formulation is applied to a particular geometry, such as a pipe or channel, the generic structure must be matched onto an external flow expressed in terms of variables relevant to the particular flow. The range of validity of the structure we find depends on the global flow properties, but we note that in turbulent shear flows the wake region which is the upper bound for the logarithmic layer is typically located where $y = y_l \gtrsim 10^3$. We write $\epsilon = y_l^{-1}$ and use this as a small parameter in the following asymptotic analysis. The parameter ϵ may be related to the Reynolds number of the flow if the asymptotic balance is obtained everywhere in the flow domain. However, since here we aim only to find an asymptotic solution in the logarithmic layer, we may leave ϵ as a quantity to be determined through full Navier–Stokes simulations.

The analysis below has some similarity to the Wentzel–Kramers–Brillouin theory, wherein a slow modulation effect to locally periodic solutions is incorporated by a perturbative approach. We shall shortly see that, to leading order, the description of a

locally periodic structure is unchanged from § 3 – thus, the analysis of that section provides an important building block – and at higher order some constraints for the slow evolution can be deduced. The vertical length scale of the slow evolution in our problem is $O(\epsilon^{-1})$, while we denote the typical vertical periodic cell depth (fast scale) as $O(\delta/\epsilon)$, with the relative cell depth $\delta \ll 1$. The small parameters δ and ϵ are linked through the asymptotic balance of the higher-order flow.

4.1. *The slow-scale evolution problem*

Equations (4.1) are parameter free and so we base our analysis on the assumption that the structures we seek are distributed over a large range of values of $y = O(\epsilon^{-1}) \gg 1$. The quantity ϵ is however not an arbitrarily small parameter but a quantity to be found numerically by full numerical solutions of the wall-layer equations. We will look for an array structure with the local cell depth a function of the slow variable spatial variable $Y = \epsilon y$. Thus, at the fast scale we define the phase function Φ for the locally periodic flow structure by

$$\Phi = \Theta(Y)/\delta. \tag{4.2}$$

The above choice of scale means that the vertical derivative is transformed as

$$\partial_y \to \frac{\epsilon \Theta_Y}{\delta}\partial_\Phi + \cdots \tag{4.3}$$

so that the cell depth at a large height y in wall units is $O(\delta/(\epsilon\Theta_Y))$. For that reason, we will refer to Θ_Y as the vertical wavenumber. We shall see from a higher-order analysis that $\delta = \epsilon^{2/5}$ is the appropriate distinguished limit.

We now consider a slowly varying distributed VWI array driven by an infinite set of waves of different streamwise wavenumbers moving downstream with the local mean flow speed at the location $Y = Y_n$. The mean part of the flow is predominantly in the x direction. In terms of the phase variable Φ, the waves have critical layers located at $\Phi = \Phi_n = \Theta(Y_n)/\delta$ where $\Phi_{n+1} - \Phi_n = 1$. We further assume that the nth wave has streamwise wavenumber $\alpha(Y_n)$. Note here that we are not considering a single wave with its wavenumber varying in the Y direction but an infinite set of distinct waves with wavenumber assigned using the function $\alpha(Y)$. Since the local array structure has a roll–streak–wave flow with variations in all three directions on the same scale we write $(X, Z) = (\epsilon/\delta)(x, \beta z)$, and on the basis of the above discussion we look for a roll–streak flow of the form (see H18 also)

$$u = \frac{\overline{u}(Y)}{\epsilon} + \frac{\delta \overline{u}_Y}{\epsilon\Theta_Y}\{U_1(\Phi, Y, Z) + \delta U_2(\Phi, Y, Z) + \cdots\} + \sum_{n=-\infty}^{\infty} u_w^{(n)}, \tag{4.4a}$$

$$v = \frac{\epsilon\Theta_Y}{\delta}\{V_1(\Phi, Y, Z) + \delta V_2(\Phi, Y, Z) + \cdots\} + \sum_{n=-\infty}^{\infty} v_w^{(n)}, \tag{4.4b}$$

$$w = \frac{\epsilon\Theta_Y}{\delta}\{W_1(\Phi, Y, Z) + \delta W_2(\Phi, Y, Z) + \cdots\} + \sum_{n=-\infty}^{\infty} w_w^{(n)}, \tag{4.4c}$$

$$p = Kx + \left(\frac{\epsilon\Theta_Y}{\delta}\right)^2\{P_1(\Phi, Y, Z) + \delta P_2(\Phi, Y, Z) + \cdots\} + \sum_{n=-\infty}^{\infty} p_w^{(n)}, \tag{4.4d}$$

where K represents a streamwise pressure gradient driving the laminar flow, assumed to be smaller than $O(\epsilon)$ when measured in wall units. We shall shortly see that the solvability condition is needed for the terms with subscript 2. Components $(u_w^{(n)}, v_w^{(n)}, w_w^{(n)}, p_w^{(n)})$ represent the nth wave. In particular, the wave pressure takes the form

$$p_w^{(n)} = \bar{u}_Y^{5/6} \left(\frac{\epsilon \Theta_Y}{\delta} \right)^{1/3} \rho_1(Y) E^{(n)} p_1(\Phi - \Phi_n, Y, Z) + \text{c.c.} + \cdots, \tag{4.4e}$$

where

$$E^{(n)} = \exp\left\{ \mathrm{i}X - \mathrm{i}\alpha(Y_n) \left(\frac{\bar{u}(Y_n)}{\delta} \right) t \right\}. \tag{4.5}$$

Here ρ_1 is the amplitude of the wave, which is chosen so that the shear associated with the roll field is modified at leading order when crossing the critical layer; the procedure is essentially identical to that described in detail in Hall & Sherwin (2010).

The scalings in (4.4) were motivated as follows. First, the scaling of the mean flow $\bar{u}$ is chosen so that it is consistent to the base flow $\bar{u} = y$. The factor $(\epsilon \Theta_Y)/\delta$ in the roll expansions are introduced so that, in view of (4.3), the roll advection term balances to the viscous term. The need for the factor $(\delta \bar{u}_Y)/(\epsilon \Theta_Y)$ in the streak expansion can be seen by considering the mean flow equation, assuming that to leading order it is driven by the nonlinear interaction of the roll and the streak. The origin of the wave scaling is less obvious as it involves the critical layer analysis; however, the essential mechanism that is determined so that the wave drives the roll–streak is unchanged from the usual VWI. The derivation of the scaling (4.4*e*) is explained in detail in the appendix. For simplicity in the above expansion, we have assumed that each cell is maintained by a single wave. If, say, two waves are involved we must, as previously noted in § 2.1, split the contributions into two sums and allow for the wave speeds of each wave to differ from the mean flow speed at the middle of each cell. The more general case is easily accounted for by replacing the summation terms in (4.4) into two sums and inserting a wave speed into (4.5).

The factors dependent on $\Theta_Y, \bar{u}_Y$ in (4.4) have been introduced in order to facilitate comparison with the uniform shear case described in § 2. Owing to those factors, at leading order the roll–streak–wave flow satisfies the triply periodic canonical array problem (2.6)–(2.8*a*,*b*) but with y replaced by Φ, as shown in H18. In order to do so the local effective wavenumbers and the global wavenumbers must be related as

$$(\alpha^\dagger, \beta^\dagger) = \left(\frac{\alpha}{\Theta_Y}, \frac{\beta}{\Theta_Y} \right), \tag{4.6}$$

in which case

$$\begin{gathered} \boldsymbol{U}_1(\Phi, Y, Z; \alpha, \beta, \Theta_Y, \bar{u}_Y) = \boldsymbol{U}(\Phi, Z; \alpha^\dagger, \beta^\dagger), \\ p_1(\Phi - \Phi_n, Y, Z; \alpha, \beta, \Theta_Y, \bar{u}_Y) = \tilde{p}(\Phi - n, Z; \alpha^\dagger, \beta^\dagger) \equiv \tilde{p}^{(n)}(\Phi, Z; \alpha^\dagger, \beta^\dagger), \\ \rho_1(Y; \alpha, \beta, \Theta_Y, \bar{u}_Y) = \rho(\alpha^\dagger, \beta^\dagger), \end{gathered}$$

together with similar expressions for the wave velocity field. The left-hand sides of these equations are the quantities appearing in the expansions (4.4), while on the right-hand side the solution of the canonical equations (2.7) are used. The implication is that hereafter we can remove the subscripts 1 which appear in the expansions (4.4).

We note at this stage that $\overline{u}_Y(Y)$ and the normal and streamwise wavenumbers $\Theta_Y(Y), \alpha(Y)$ are all unknown and it is of interest to know how many of these functions can be specified *a priori*. If we think of the array being formed by the bringing together of the vertically localised canonical states of Blackburn *et al.* (2013) then it might be anticipated that, certainly for large separations, the normal wavenumber $\Theta_Y(Y)$ should be at our disposal. We might anticipate that the mean flow function is then fixed to be the function supporting that solution leaving α also to be chosen. However, we shall shortly see that when the flow in each cell strongly interacts, there are two constraints on the slow dynamics. It will turn out that here, unlike in H18, only one of $\Theta_Y(Y), \alpha(Y), \overline{u}_Y(Y)$ can be chosen.

Hall (2018) obtained the first constraint by considering the development of $\overline{u}$. Integrating the streamwise momentum equation over one periodic cell $(X, \Phi, Z) \in [0, 2\pi] \times [0, 1] \times [0, 2\pi]$, we obtain

$$\overline{u}_{YY} + (\overline{u}_Y \sigma)_Y = 0. \tag{4.7}$$

The function $\sigma = -\langle UV \rangle$, where $\langle\,\rangle$ denotes the average over $0 < \Phi < 1$, $0 < Z < 2\pi$, can be obtained by the leading-order problem (see (3.6)) and depends on the slow variable Y through $\alpha^\dagger, \beta^\dagger$. As pointed out in H18, (4.7) is essentially the RANS equation for the mean flow but with the only difference that here the mean is taken over X, Φ, Z rather than X, Z. At this stage, in the absence of slow time dependence, one of the functions $\overline{u}_Y(Y), \Theta_Y(Y), \alpha(Y)$ is fixed, and in H18 no further constraint was enforced.

We shall see below that in fact the second constraint is available by consideration of the higher-order equations for wave, roll and streak. The slow dependence on Y of the leading-order roll–streak flow is through the different slow amplitude functions multiplying each quantity and through the local wavenumbers $\alpha^\dagger, \beta^\dagger$. As is usual with the phase equation approach, the slow variation will be constrained at next order through a solvability condition.

As observed earlier, the nature of the wave field sustaining the locally periodic roll–streak structure differs according to the symmetries to be imposed. For simplicity, here we assume that (i) just one dominant sustaining wave is present in each cell and (ii) the local roll–streak field possesses the mirror symmetry mentioned in § 3.1. With this symmetry, we can assume that the critical layer is flat and located at $Y = Y_n$. Furthermore, this allows us to significantly contract the algebra that is needed in the higher-order critical layer analysis (see the appendix) to derive the solvability condition.

At next order the slow variation of the roll–streak with respect to Y comes into play, and it is $O(\delta)$ smaller than the leading-order effect. We also remark that even when there is no slow effect in the flow there are some higher-order terms in the VWI. The size of the second type of higher-order terms are comparable to the critical layer thickness, which is the largest perturbative parameter in the asymptotic analysis. The critical layer analysis shown in the appendix reveals that the layer thickness is $O((\epsilon/\delta)^{2/3})$, and by balancing the two perturbative effects, we have the distinguished limit $\delta = \epsilon^{2/5}$. Collecting the terms of this size, the second-lowest-order roll–streak equations are written as

$$(\mathbb{A} + \mathbb{B} + \mathbb{C} + \mathbb{D} + \mathbb{E})\boldsymbol{X} = \boldsymbol{F}, \tag{4.8}$$

where $\boldsymbol{X}$, $\mathbb{A}$, $\mathbb{B}$, $\mathbb{C}$, $\mathbb{D}$, $\mathbb{E}$ are defined by

$$\boldsymbol{X} = \begin{bmatrix} U_2 \\ V_2 \\ W_2 \\ P_2 \end{bmatrix}, \quad \mathbb{A} = \begin{bmatrix} \dfrac{\partial^2}{\partial \Phi^2} + \beta^{\dagger 2}\dfrac{\partial^2}{\partial Z^2} & 0 & 0 & 0 \\ 0 & \dfrac{\partial^2}{\partial \Phi^2} + \beta^{\dagger 2}\dfrac{\partial^2}{\partial Z^2} & 0 & 0 \\ 0 & 0 & \dfrac{\partial^2}{\partial \Phi^2} + \beta^{\dagger 2}\dfrac{\partial^2}{\partial Z^2} & 0 \\ 0 & 0 & 0 & 0 \end{bmatrix},$$

$$\mathbb{B} = \begin{bmatrix} -V\dfrac{\partial}{\partial \Phi} & 0 & 0 & 0 \\ 0 & -V\dfrac{\partial}{\partial \Phi} & 0 & 0 \\ 0 & 0 & -V\dfrac{\partial}{\partial \Phi} & 0 \\ 0 & \dfrac{\partial}{\partial \Phi} & 0 & 0 \end{bmatrix},$$

$$\mathbb{C} = \begin{bmatrix} -\beta^{\dagger} W\dfrac{\partial}{\partial Z} & 0 & 0 & 0 \\ 0 & -\beta^{\dagger} W\dfrac{\partial}{\partial Z} & 0 & 0 \\ 0 & 0 & -\beta^{\dagger} W\dfrac{\partial}{\partial Z} & 0 \\ 0 & 0 & \beta^{\dagger}\dfrac{\partial}{\partial Z} & 0 \end{bmatrix},$$

$$\mathbb{D} = \begin{bmatrix} 0 & -U_\Phi - 1 & 0 & 0 \\ 0 & -V_\Phi & 0 & 0 \\ 0 & -W_\Phi & 0 & 0 \\ 0 & 0 & 0 & 0 \end{bmatrix}, \quad \mathbb{E} = \begin{bmatrix} 0 & 0 & -\beta^{\dagger} U_Z & 0 \\ 0 & 0 & -\beta^{\dagger} V_Z & 0 \\ 0 & 0 & -\beta^{\dagger} W_Z & 0 \\ 0 & 0 & 0 & 0 \end{bmatrix}.$$

The term $\boldsymbol{F} = [F_1, F_2, F_3, F_4]^{\mathrm{T}}$ on the right-hand side of (4.8) arises from the slow variation of the coherent structure with Y and is given by

$$F_1 = \frac{\bar{u}_{YY}}{\Theta_Y \bar{u}_Y}(UV - 2U_\Phi) + \frac{\Theta_{YY}}{\Theta_Y^2}(U_\Phi - UV) + \frac{1}{\Theta_Y}(VU_Y - 2U_{Y\Phi}), \tag{4.9a}$$

$$F_2 = \frac{\Theta_{YY}}{\Theta_Y^2}(V^2 - 3V_\Phi + 2P) + \frac{1}{\Theta_Y}(P_Y - 2V_{Y\Phi} + VV_Y) + f_2, \tag{4.9b}$$

$$F_3 = \frac{\Theta_{YY}}{\Theta_Y^2}(VW - 3W_\phi) + \frac{1}{\Theta_Y}(VW_Y - 2W_{Y\Phi}) + f_3, \tag{4.9c}$$

$$F_4 = -\frac{\Theta_{YY}}{\Theta_Y^2}V - \frac{1}{\Theta_Y}V_Y. \tag{4.9d}$$

Here

$$f_2 = \sum_{n=-\infty}^{\infty} \frac{\Theta_Y^{2/3}}{\bar{u}_Y^{1/3}\alpha^{\dagger 2}} \left\{ \left(\frac{|\tilde{p}_\Phi^{(n)}|^2}{(\Phi+U)^2} \right)_\Phi + \beta^\dagger \left(\frac{\beta^\dagger \tilde{p}_\Phi^{(n)} \tilde{p}_Z^{(n)*}}{(\Phi+U)^2} \right)_Z \right\} + \text{c.c.},$$

$$f_3 = \sum_{n=-\infty}^{\infty} \frac{\Theta_Y^{2/3}}{\bar{u}_Y^{1/3}\alpha^{\dagger 2}} \left\{ \left(\frac{\beta^\dagger \tilde{p}_\Phi^{(n)} \tilde{p}_Z^{(n)*}}{(\Phi+U)^2} \right)_\Phi + \beta^\dagger \left(\frac{\beta^{\dagger 2} |\tilde{p}_Z^{(n)}|^2}{(\Phi+U)^2} \right)_Z \right\} + \text{c.c.},$$

are associated with the wave Reynolds stress outside of the critical layer. The above perturbed roll–streak equations must once again be solved subject to periodicity in Z. We do not write down the perturbed wave pressure equation because it is readily shown that, whatever the symmetries, the perturbed wave pressure equation does not enter the perturbed jump conditions and so we need not consider it here.

We see that the normal and spanwise momentum equations are independent of the streamwise momentum equation in (4.8), just as was the case for (2.7). The link between the roll and streak equations must therefore come from the jump conditions. For the mirror-symmetric mode, we can take the critical layers to be at $\Phi = 0, \pm 1, \pm 2, \ldots$ and so the boundary conditions in Φ can be most conveniently written in the form

$$\begin{gathered} U_2(1,Z) = U_2(0,Z), \quad U_{2\Phi}(1,Z) = U_{2\Phi}(0,Z), \\ V_2(1,Z) = V_2(0,Z), \quad V_{2\Phi}(1,Z) = V_{2\Phi}(0,Z), \\ W_{2\Phi}(1,Z) = W_{2\Phi}(0,Z), \end{gathered}$$

and

$$W_2(0,Z) - W_2(1,Z) = \beta^\dagger \left\{ \frac{U_2(0,Z)\hat{J}(Z)}{1+U_\Phi(0,Z)} \right\}_Z, \tag{4.10}$$

where the jump is derived in (A13) and $\hat{J}(Z)$ is the function defined in (2.10*a–c*).

The crucial point here is that the homogeneous form of (4.8) and the associated boundary conditions now has a solution $(U_2, V_2, W_2, P_2) = \partial_\Phi(U, V, W, P)$ representing the translational invariance of the roll–streak flow. The outcome is that the inhomogeneous problem specified by (4.8) and the associated boundary conditions require a solvability condition to be satisfied; in the usual manner this is done by constructing the system adjoint to the homogeneous problem. The adjoint is formed by multiplying the homogeneous form of (4.8) by the adjoint function $\boldsymbol{S} = [S_1, S_2, S_3, S_4]^{\mathrm{T}}$ and integrating over $0 < \Phi < 1$, $0 < Z < 2\pi$ and integrating by parts. We find that the adjoint function must satisfy the equation

$$(\mathbb{A} - \mathbb{B} - \mathbb{C} + \mathbb{D}^{\mathrm{T}} + \mathbb{E}^{\mathrm{T}})\boldsymbol{S} = \boldsymbol{0}, \tag{4.11}$$

together with the boundary conditions

$$\begin{gathered} S_1(1,Z) = S_1(0,Z), \quad S_{1\Phi}(1,Z) = S_{1\Phi}(0,Z), \\ S_2(1,Z) = S_2(0,Z), \quad S_{2\Phi}(1,Z) = S_{2\Phi}(0,Z), \\ S_3(1,Z) = S_3(0,Z), \quad S_{3\Phi}(1,Z) = S_{3\Phi}(0,Z). \end{gathered}$$

Moreover, S_1, S_2 are odd, S_3, S_4 are even with respect to the $\Phi = 0$ axis.

The solvability condition then takes the form

$$0 = \sum_{k=1}^{k=4} \langle S_k F_k \rangle. \tag{4.12}$$

Here we note that there is no energy input for S_1 in (4.11) and, thus, $S_1 \equiv 0$. Further using (4.9) and the fact that β is constant, (4.12) may be written in the form

$$e_1 \left(\frac{\alpha}{\Theta_Y} \right)_Y + e_2 \left(\frac{\beta}{\Theta_Y} \right)_Y + e_3 \frac{\Theta_{YY}}{\Theta_Y} = 0, \tag{4.13}$$

which is the second constraint of our interest. Here e_1, e_2, e_3 are defined by

$$e_1 = \langle S_2(VV_{\alpha^\dagger} - 2V_{\alpha^\dagger} + P_{\alpha^\dagger}) + S_3(VW_{\alpha^\dagger} - 2W_{\Phi\alpha^\dagger}) + S_4 V_{\alpha^\dagger} \rangle, \tag{4.14a}$$

$$e_2 = \langle S_2(VV_{\beta^\dagger} - 2V_{\beta^\dagger} + P_{\beta^\dagger}) + S_3(VW_{\beta^\dagger} - 2W_{\Phi\beta^\dagger}) + S_4 V_{\beta^\dagger} \rangle, \tag{4.14b}$$

$$e_3 = \langle S_2(V^2 - 3V_\Phi + 2P) + S_3(VW - 3W_\Phi) + S_4 V \rangle, \tag{4.14c}$$

and are functions of the slow variable Y through its dependence on $\alpha^\dagger$, $\beta^\dagger$. Note that by symmetry f_2 and f_3 do not contribute to the solvability. In the above set of equations, the subscripts $\alpha^\dagger$, $\beta^\dagger$ denote the derivative with respect to the local wavenumbers and, hence, in principle, the integrand can be computed by a parameter search of the local solutions and the solution of the adjoint problem (4.11).

Although the evolution (4.13) has been derived for the mirror-symmetric mode, the essential structure of the equation is unchanged for other symmetries. In any case, the evaluation of the integrals appearing in the definitions above requires the solution of the adjoint partial differential equations. That rather daunting calculation is not discussed here but in the next section, where we will see that important conclusions regarding the possibility of a totally self-similar state consistent with the attached eddy hypothesis can be drawn without doing so.

We now have sufficient information to see how the canonical vertically localised states may be moved close enough together for them to interact. We recall that we have three unknown functions u_Y, Θ_Y, α and the two evolution equations (4.7) and (4.13) linking those functions. If we think of each VWI cell as being initially far away from its neighbours to interact it seems most natural to determine how the mean flow $\overline{u}$ and wavenumber distribution change in order to support the mutual interaction. In other words, it is perhaps more natural to specify Θ_Y and determine $\overline{u}_Y, \alpha$ from the two evolution equations.

4.2. *Self-similar coherent structures with logarithmic mean flow profile*

Here we shall explore the role of the VWI arrays in the logarithmic layer by seeking self-similar distributed solutions consistent with the attached eddy hypothesis. Firstly we note that the attached eddy hypothesis requires that the dominant streamwise and spanwise wavelengths vary linearly with distance from the wall. The apparently insurmountable constraint not permitting self-similarity is that the spanwise wavenumber β is a constant so the spanwise variation cannot be self-similar with respect to Y. So at first consideration it appears that the slowly varying distributed structures we have constructed are not consistent with the hypothesis; the key to the resolution is the consideration of the local VWI array solutions fully isolated in the spanwise direction. Thus, we will see that self-similarity is achieved when the spanwise variations of the roll–streak structure are no longer influenced by the distant periodic constraint in the spanwise direction.

We have already seen such isolated solutions indeed exist in § 3.2, and confirmed that their flow structure becomes insensitive to the change of $\beta^\dagger$ for any choice of sufficiently small $\beta^\dagger$. First we note that from the invariance of the isolated flow structure against $\beta^\dagger$, we can derive the asymptotic properties

$$\sigma \to \beta^\dagger \sigma_0(\alpha^\dagger), \quad \frac{e_1}{e_3} \to B_1(\alpha^\dagger), \quad \frac{e_2}{e_3} \to \frac{B_2(\alpha^\dagger)}{\beta^\dagger} \tag{4.15a–c}$$

as $\beta^\dagger \to 0$. The scaling law for σ is essentially the mean flow scaling found in Deguchi *et al.* (2013), where the asymptotic behaviour was observed for $\beta^\dagger$ numerically smaller than unity. It can be deduced by recalling that $\sigma = -\langle UV \rangle$, where $\langle\,\rangle$ denotes the average over the periodic box. If UV is only non-zero for an $O(1)$ spanwise region of the domain and the rest of $O(1/\beta^\dagger)$ region does not contribute to the average, obviously the scaling above is expected. The other two scaling laws can be similarly deduced from (4.14).

Noting that complete self-similarity in the global problem is only achieved if the local streamwise wavelength is everywhere constrained such that $\alpha^\dagger$ is a constant, we find that in the limit (4.15*a–c*) the evolution (4.7) and (4.13) reduce to

$$\overline{u}_{YY} + \sigma_0 \beta \left(\frac{\overline{u}_Y}{\Theta_Y} \right)_Y = 0, \tag{4.16}$$

$$(1 - B_2) \frac{\Theta_{YY}}{\Theta_Y} = 0, \tag{4.17}$$

respectively. From the second evolution (4.17) we see that the self-similar roll–streak field is possible only if

$$B_2(\alpha^\dagger) = 1, \tag{4.18}$$

which fixes the values of $\alpha^\dagger$ permitting self-similarity. If the flow is to be consistent with the attached eddy hypothesis, then the cell depth must locally scale linearly in Y. Thus, we choose the vertical wavenumber

$$\Theta_Y = 1/(Y - Y_0), \tag{4.19}$$

assuming that the self-similarity begins at $Y = Y_0$. For spanwise-isolated local solutions, whatever the value of $\beta^\dagger$ is, the typical streamwise and spanwise scales are comparable to the depth of the vertical domain. Thus, (4.19) implies that in the global problem the cell depth and the typical spanwise and streamwise length scales of the equilibrium structure all vary like $Y - Y_0$, and, hence, the size variation of the VWI array is the same as envisaged in the attached eddy hypothesis.

Given a choice of $\Theta(Y)$ and a spanwise-isolated solution of the canonical VWI array problem, we are able to construct a self-similar solution in terms of the wall-unit variables y, z. As an illustrative example, in figure 7 we show the global flow structure inferred by the local leading-order solution seen in figure 4 and the distribution $\Theta = \ln Y$. In order to explain how that picture was generated, let us write (y, z) used in §§ 2 and 3 as $(\hat{y}, \hat{z})$ to avoid confusion. The choice of Θ means that $\Theta_Y = Y^{-1}$, i.e. $Y_0 = 0$ in (4.19) and the self-similarity begins at $y = 0$. From (4.6), the local wavenumber varies like $\beta^\dagger = \beta Y$. Further using the two definitions of Z introduced in §§ 2 and 4, we have the relationship $Z = (\epsilon^{\frac{3}{5}})\beta z = \beta^\dagger \hat{z} = \beta \epsilon y \hat{z}$, while for the vertical coordinate, we can simply

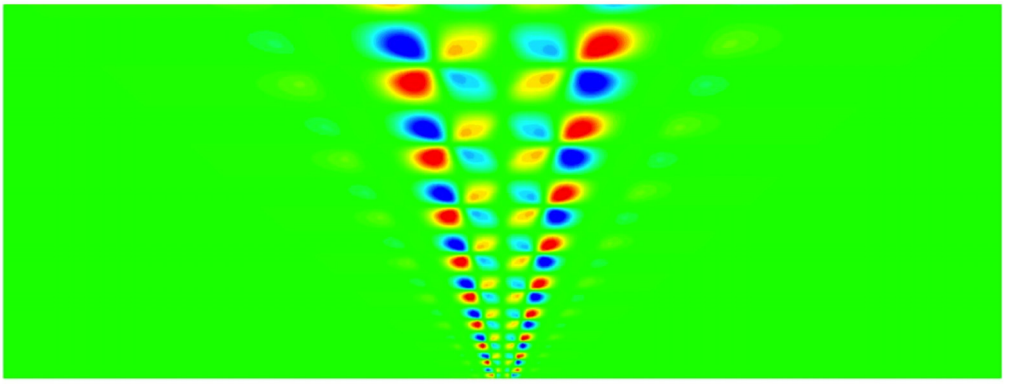

Figure 7. The roll stream function of the self-similar solution in the wall-unit coordinate (y, z). The isolated solution shown in figure 4 is used together with $\Theta = \ln Y$ and $\epsilon = 0.001$. The horizontal coordinate is $z \in [0, 1200]$, the vertical coordinate is $y \in [50, 500]$.

use the definition of Φ (which equals $\hat{y}$) to deduce

$$\hat{y} = \frac{\ln y}{\epsilon^{\frac{2}{5}}}, \quad \hat{z} = \frac{z}{\epsilon^{\frac{2}{5}} y},$$

from which we can find the flow at any point in the y–z plane through the local array solution at $(\hat{y}, \hat{z})$. As may be seen in figure 4, self-similarity consistent with the attached eddy hypothesis can indeed be reached with the isolated solutions.

Note that we have not solved for the adjoint problem and so we can only assume here that the condition (4.18) may be achieved at some $\alpha^\dagger$. On the assumption that $\alpha^\dagger$ satisfying (4.18) exists, the mean flow (4.16) can be integrated to yield

$$\overline{u}(Y) = C_1 \ln\left(Y - Y_0 + \frac{1}{\sigma_0 \beta}\right) + C_2, \tag{4.20}$$

where C_1, C_2 are integration constants.

Therefore, by writing the mean part of u as $u_m(y) = \epsilon^{-1}\overline{u}(Y)$, we can see that the self-similar VWI array leads naturally to the Kármán law of the wall

$$u_m(y) = \frac{1}{\kappa} \ln y + C, \tag{4.21}$$

in which we have chosen

$$Y_0 = \frac{1}{\sigma_0 \beta}. \tag{4.22}$$

We remark here that this choice and the linear wall-normal variation of the eddy length scale are assumptions to yield the log-law, although they seem physically reasonable. The use of those assumptions may conversely be justified by certain special scale invariances of the logarithmic profile, e.g. as noted in Moarref *et al.* (2013) and H18, but we do not go into detail here.

The Kármán constant κ appearing in (4.21) may be found by solving the matching problem which connects the solution in what we believe to be the logarithmic layer to the adjacent regions such as the buffer and/or wake layers. The conclusion is therefore that our self-similar VWI structure does lead to the law of the wall, but the associated

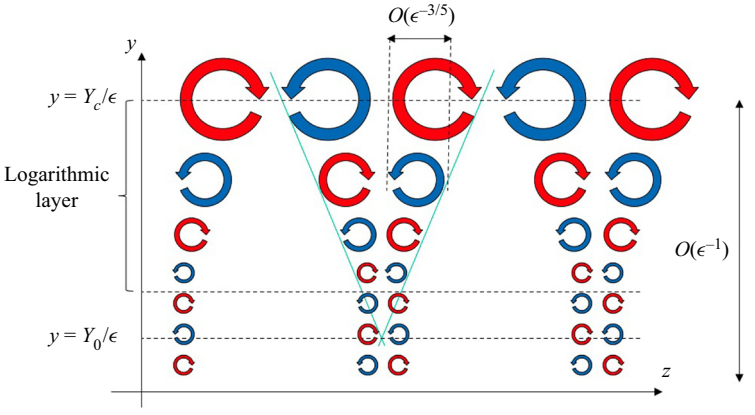

Figure 8. Schematic of coherent structures in near-wall turbulent boundary layers, with distances given in wall units. The self-similar VWI eddies of size $O(\epsilon^{-3/5})$ produce a logarithmic mean flow profile in a layer of depth $O(\epsilon^{-1})$. At the lower bound of the logarithmic layer, the eddy size reaches the Kolmogorov microscale $O(1)$. At the other bound $y = Y_c/\epsilon$, isolated eddies begin to interact with each other and, thus, self-similarity must be destroyed. The global flow has a spanwise period $2\pi/\beta\epsilon^{3/5}$.

value of the Kármán constant can only be fixed by a more complete matched asymptotic expansion of the entire flow. This outcome is slightly disappointing but the structure we have constructed is arguably the first nonlinear equilibrium state built from slowly varying SSP or VWI states shown to be consistent with the law of the wall and the attached eddy hypothesis.

Although such a matching problem is out of the scope of the present study, it is nevertheless interesting to see how the self-similar structure breaks down on exiting the logarithmic layer. As remarked earlier, the self-similarity starts at $Y = Y_0$ meaning that the roll cell size formally shrink to zero there; see figure 8. However, the VWI theory breaks down before reaching this position. When the roll cell size becomes $O(1)$ in the wall unit, the flow reaches the Kolmogorov microscale and, hence, the assumption used for the VWI array theory that the cell size is asymptotically large in the wall unit is not satisfied. Since the size of the roll cell varies like $(\delta/\epsilon)(Y - Y_0)$, the VWI array is terminated at slightly ($O(\epsilon^{3/4})$ in Y) above the location $Y = Y_0$. The small-scale flows may persist all the way down to the viscous sublayer, and here the localised solutions at the Kolmogorov microscale found by Deguchi (2015), Eckhardt & Zammert (2018) and Yang *et al.* (2019), or their distributed form, (see Yang, Willis & Hwang 2018) would be relevant.

The opposite end of the logarithmic region can be found by recalling that in the canonical VWI array problem localisation is possible only when $\beta^\dagger$ is sufficiently small (i.e. the spanwise dimension of the periodic box is large in the local problem). Thus, when $\beta^\dagger$ becomes sufficiently large and reaches a critical value, $\beta_c^\dagger$ say, the spanwise-isolated coherent structures originally placed at a large distance apart begin to interact with each other. If this saturation occurs in the global problem the flow should deviate from the self-similar state and, hence, the wake region may appear. Since the local wavenumber varies like $\beta^\dagger = \beta(Y - Y_0)$, the vertical position in Y at which the self-similarity halts can be estimated as

$$Y_c = Y_0 + \frac{\beta_c^\dagger}{\beta} = (1 + \sigma_0\beta_c^\dagger)Y_0. \tag{4.23}$$

Here we recall that the slow evolution equations imply that the vertical mean flow variation is determined by the wavenumber dependence of the local solution, and we used the asymptotic behaviour of the isolated solution in the limit of $\beta^\dagger \to 0$ to deduce the logarithmic mean flow profile. Thus, if the isolated structure were only occurring in an extremely wide box, so that $\beta_c^\dagger$ is extremely small, the depth of the logarithmic layer would have been very thin, as expected from (4.23). This is not the case at least for the isolated solution shown in figure 4, where $\sigma_0 \approx 0.437$ and $\beta_c^\dagger \approx 1.5$ yield the ratio $Y_c/Y_0 \approx 1.66$. This number is still not too large, but we note that the isolated solution on which we have based the above discussion would not be the only possible isolated state of the canonical VWI array problem. The ratio also depends on σ_0. The main reason why that value is not so large for our solution is that the coherent structure possesses the character of the typical lower-branch solutions (see figure 4). However, in view of the substantial evidence of the existence of uniform momentum zones in near-wall turbulence (Meinhart & Adrian 1995; Adrian, Meinhart & Tomkins 2000), there may also be isolated solutions of the upper-branch type, and they would play more major roles in the flow dynamics. For such upper-branch-type solutions, as seen in figure 5, the momentum transfer σ is much larger, and, hence, the logarithmic law will be valid for a wider range of Y.

5. Discussion and conclusions

We have found a number of connections between the VWI array theory and multiple-scale coherent structures typically seen in near-wall turbulent boundary layers. The coherent structures at a local position can be found by the canonical triply periodic problem, defined in § 2, that exactly corresponds to the high-Reynolds-number limit of the shearing box problem. The global distribution of the vortex array can be determined through the multiple-scale analysis developed in § 4. Unlike other turbulent flow analyses only a few assumptions are employed, the main assumptions being the largeness of the Reynolds number and the travelling wave form of the local coherent structures. The model is fully nonlinear and there is a strong interaction between the coherent structures and mean flow. Therefore, the key significance of the distributed VWI structure discussed in H18 and herein is that it is the first closed large-Reynolds-number Navier–Stokes-based analysis of near-wall coherent structures. The main outcome of the analysis is that the overall mean state in which the structure develops is fixed by its slow dynamics so that the shape of the mean profile is determined by the nature of the interaction.

In § 3 we demonstrated that the canonical triply periodic VWI problem has various solutions with character typical of coherent structures observed in a number of previous shear flow studies. Two symmetries were used; the first symmetry used is the mirror-symmetric mode that can be captured by imposing (3.2) and the vertical periodic condition to the roll–streak part, so that the generated wave satisfies the symmetries seen in the plane Couette flow counterpart (3.1). The symmetry (3.2) naturally yields flat critical layers as observed in the plane Couette solution of Itano & Generalis (2009), EQ7/EQ8 of Gibson *et al.* (2009), and indeed implemented in the limited numerical VWI array results given in H18.

For the second symmetry, here referred to as the sinuous mode, the wave possesses spanwise-wavy critical layers, known to be relevant for the more dynamically important kind of coherent structures (e.g. the Nagata–Busse–Clever solution in plane Couette flow). To generate the sinuous-type coherent structures, only the first two roll–streak symmetries ((3.2*a*), (3.2*b*)) are imposed, together with the shifted periodic condition (3.3). The periodic VWI array produced in that process has four periodic counter-rotating cells in two

fundamental boxes corresponding to one spanwise and one vertical wavelength, meaning that it is equivalent to a VWI description with two waves present in each periodic cell.

Here let us briefly consider the role of the vertical phase shift of the roll cells in more detail. Suppose we imagine an infinite array of VWI states spaced equally in the y direction but sufficiently far apart that they do not interact with each other, as seen in Blackburn *et al.* (2013). If the distance between the coherent structures is decreased there will be a mutual strong nonlinear interaction between them and the nature of the interaction will depend on the relative spanwise phase of neighbouring cells. If the separation of the coherent structures is sufficiently large then, whatever the spanwise distribution of the phases, there will always be a solution of the associated distributed VWI problem. However, it is possible that as the separation decreases the possible distributions of spanwise phases will change. The sinuous-mode scenario corresponds to the rolls initially having a phase difference of π between them so that as the rolls approach each other there is less interference between the cells. However, there is no reason to suppose there are many other possible structures associated with particular phase distributions. The measurements in turbulent shear flows, see, for example, Hutchins & Marusic (2007), showing that the spanwise phase varies with both time and y, suggests the possible existence of VWI arrays in which the spanwise phase varies periodically in time.

Another possibility exists, in which there is no phase difference between neighbouring cells when they are initially far apart. As the cells become closer, the roll–streak flows connect and the most relevant natural symmetries to be satisfied are ((3.2*a*), (3.2*b*)) with the usual vertical periodic condition (3.2*c*). Our fixed-point iteration solver with those symmetries generates contours of the streak flow that take on a chevron-type pattern reminiscent of that seen in the shearing box computation of Sekimoto & Jiménez (2017). A representative solution for the chevron mode at $\alpha^\dagger = 2$, $\beta^\dagger = \pi$, $R_f = 10 \times 10^3$ is shown in figure 9. We note that this is a case in which the influence of the wave Reynolds stress extends beyond the central computational module and, for these computations, we have chosen $N = 1$, such that each roll experiences driving from three waves (see § 2.2). The remarkable similarity of the profile given in figures 9 and 3 of Sekimoto & Jiménez (2017) may reinforce our finding in the present work that at high Reynolds numbers the periodic shearing box model reduces to the VWI array structure proposed in H18. However, there is a caveat to our solution; unfortunately, the numerical convergence of the chevron mode is not as good as for the mirror-symmetric and sinuous modes. A similar difficulty was experienced in the Navier–Stokes computation of the shearing box solution, and this is partially the reason why the Smagorinsky turbulence model was used in Sekimoto & Jiménez (2017). Whether our quasi-solution gives a quantitative prediction of the full Navier–Stokes solution is also an open issue.

As summarised in § 1, it has become apparent in recent years that numerically exact solutions of the Navier–Stokes equations identified by numerical and/or asymptotic techniques play key roles in both the processes by which a flow becomes turbulent and the nature of the ensuing fully developed turbulence. Therefore, the various solutions found in § 3 may be regarded as fundamental building blocks with which to understand near-wall coherent structures seen in many experiments. Despite the reduced form of the locally periodic VWI problem derived from the Navier–Stokes equations, results presented in § 3 reveal that its solutions possess surprisingly rich patterns. The patterns found here remarkably include characteristics typical of near-wall turbulent coherent structures such as spatial intermittency and uniform momentum zones, thereby suggesting that the VWI problem has enough structure to describe many key aspects of near-wall turbulence, e.g. observed by Meinhart & Adrian (1995), Adrian *et al.* (2000), de Silva *et al.* (2016, 2017) and Laskari *et al.* (2018).

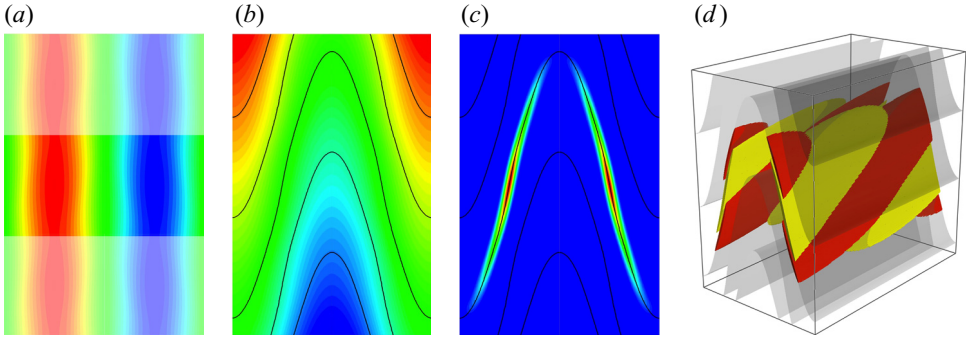

Figure 9. A lower-branch solution for the chevron mode at $\alpha^\dagger = 2$, $\beta^\dagger = \pi$, $R_f = 10 \times 10^3$. Panels as for figure 2.

In Deguchi & Hall (2014*c*) the emergence of the homogenised zone in the numerical equilibrium solution of plane Couette flow was briefly explained by using the Prandtl–Batchelor theorem (Batchelor 1956). When the convective effect in the roll–streak equations dominates the viscous effect, it is straightforward to show that in the region where the roll streamline is closed the values of the total streak $(y + U)$ and the roll vorticity $(V_z - W_y)$ become constant. Since, strictly speaking, such a homogenisation cannot be realised in the VWI framework owing to the assumed convective–viscous balance in the roll–streak, whether or not a relevant new asymptotic regime exists is an open question. A clean analytic roll solution in the homogenised zone can be found in a manner similar to the natural convection problem, e.g. analysed by Robinson (1967), and certainly that is consistent with the numerical observation. However, an identification of the precise mechanism by which the strong roll circulation is driven by the wave activity was numerically difficult.

Recently, Montemuro *et al.* (2020) constructed a reduced model system for infinite homogeneous shear flow assuming that the Prandtl–Batchelor inertial structure is driven by very fine-scale waves generated in the shear layer between two homogenised zones. Here we remark that owing to the reasons that follow, their flow field is quite different to the typical upper-branch flow structures seen in many previous Navier–Stokes and our hybrid computations. First, in Montemuro *et al.* (2020) the wave speed is assumed to be sufficiently different from the homogenised speed such as to place the critical layer in the shear layer. However, for the upper-branch solutions, the wave speed is typically very close to the homogenised streak speed. In particular, for the sinuous mode, both speeds are zero in the central module, owing to symmetry. Second, as shown in Montemuro *et al.* (2020), the upper-branch solutions in plane Couette flow, which superficially exhibit uniform momentum zones with shear layers, do not scale with the Reynolds number; that is, the shear layers do not thin as the Reynolds number is increased and there is not strict homogenisation of the streak. In fact, these Reynolds-number-independent attributes of the streak accord perfectly with the predictions of VWI theory – but for that reason, in VWI theory perfect homogenisation does not occur. Third, Montemuro *et al.* (2020) adopted an asymptotically large streamwise wavenumber, while it is an $O(1)$ number in the VWI. One might anticipate that by increasing the streamwise wavenumber of our VWI solutions the inertial regime envisioned by Montemuro *et al.* (2020) would be achieved, but as seen in figure 5, this was not possible owing to the saddle-node point.

In § 4 the distributed VWI array problem was reformulated in localised wall-layer variables. That approach was motivated by the widely held belief that in the logarithmic

layer of turbulent shear flows, the flow is in some sense generic and not influenced by the external geometry or flow. Within the wall-unit formulation the Reynolds number is unity and so the distance from the wall serves as the large parameter in the asymptotic problem. Our asymptotic analysis is carried out in terms of a parameter $L = 1/\epsilon$ representing the depth of the fluid layer where the analysis is valid. We do not relate $\epsilon \ll 1$ to any Reynolds number associated with the flow in a particular configuration; however, it can be inferred from many experimental results that ϵ becomes smaller as Re_τ increases. We have shown in § 4.2 that when the mean pressure gradient driving the base flow is sufficiently small, i.e. K in (4.4*d*) is smaller than $O(\epsilon)$, the logarithmic law can be derived in this layer by taking the distribution of the normal wavenumber of the self-similar coherent structures as (4.19).

A potential objection to the description of near-wall flows in § 4.2 is that the mean flow momentum equation (4.7), or its alternative form (4.16), expresses a balance between gradients of viscous and Reynolds stresses and does not account for possible contributions from forcing terms such as the streamwise pressure gradient (as occurs in turbulent pipe and channel flows), or mean advection (as in zero pressure gradient boundary layers). The assumption $K \ll O(\epsilon)$ made in § 4.2 implies that we are mostly concerned with the logarithmic region near the wall where the shear stress gradient balance is dominant compared with the body force effect. This balance is relevant up to the so-called mesolayer $y^+ \sim O(\sqrt{Re_\tau})$, as demonstrated by Wei *et al.* (2005) and Klewicki (2013).

One may therefore think that the omission of body force leads to difficulty in explaining logarithmic behaviour in the regions of the outer layer more remote from the wall, since it is well established by analyses of a number of experiments and numerical computations that the mean viscous stress gradient is negligible compared with the gradient of Reynolds stress and the body force there; see, e.g. Wei *et al.* (2005). However, the objection may be surmounted by assuming $K \sim O(\epsilon)$, in which case one must add a constant (K_0, say) to the right-hand side of the mean flow (4.16). Even in this modified equation, the logarithmic law (4.21) can still be found by choosing the vertical wavenumber distribution as $\Theta_Y = 1/[K_0 Y^2/(\sigma_0 \beta C_1) + Y - Y_0]$, instead of (4.19). Interestingly, the viscous term $\overline{u}_{YY} = -C_1/Y^2$ then eventually becomes sub-dominant compared with the pressure-gradient term K_0 when Y is large, while the usual Millikan-type argument can be used for small Y, consistent with the observations made by Wei *et al.* (2005).

The basic scales and interactions in the present work remain the same as in the multiple-scale analysis by H18 but we now find a second 'master' or 'slow' equation that was not uncovered in that earlier work. The two slow equations govern the overall variation of the flow in the y direction and time, and, hence, just one of the distributions in y of the box depth, mean flow or local streamwise wavenumber needs to be specified. An important by-product in deducing the second slow evolution equation is that if the depth of the logarithmic layer measured in wall units is L, the typical size of the roll cells in the layer scales like $O(L^{3/5})$. Testing whether experimentally/numerically generated turbulence at various Reynolds numbers satisfies that scaling law may be a feasible task.

The slow equations also led us to construct a self-similar distribution of the coherent structures in the logarithmically varying mean flow consistent with the attached eddy hypothesis of Townsend (1951). Self-similarity of the coherent structures in all three spatial directions as constructed here relies on the existence of spanwise-isolated solutions in the canonical local VWI problem, as found in § 3.2. When the local sizes of such coherent structures are varied in direct proportion to distance from the wall, the associated variation of momentum transport gives a mean flow profile of logarithmic type. We remark that although our self-similar solution possesses the scalings predicted by the attached eddy hypothesis, technically the precise relation between the two sets of ideas is rather

ambiguous in the nature by which the eddies extend to the wall. The eddies which provide the name for Townsend's hypothesis are assumed to be both self-similar and attached to the wall (see, e.g. figure 1 in Hwang 2015) while our figure 8 shows eddies that are detached from the wall. As discussed by Marusic & Monty (2019), one cannot easily reconcile the notion of an infinite regression of self-similar eddies to the presence of a viscous near-wall region of finite depth.

The linear scaling of the eddies is certainly observed in wall turbulence, but the reasons why it occurs are debatable. Recently the role of the wall in the transition of the eddy size from inner scale to outer scale was studied in various meticulously configured numerical simulations. Mizuno & Jiménez (2013) used modified shear-periodic conditions to impose the vertical variation of the eddy size in the shearing box. An important implication of their result is that rather than the distance to the wall, a mixing length determined by the mean local shear determines the characteristic length scale of the eddies. More recently, Lozano-Durán & Bae (2019) arrived at a similar conclusion using modified direct numerical simulations of a channel flow. Sekimoto *et al.* (2016) showed that the local eddy structure of near-wall turbulence can be generated even in the usual shearing box simulation, if the result is suitably rescaled around the local part of the mean flow. All of the above studies result in Townsend's scaling, but the assumed eddy structure is closer to our self-similar solution rather than that originally envisaged by Townsend's hypothesis.

In the present work we have extended the asymptotic analysis of H18 to yield the asymptotic properties of the near-wall turbulent boundary layers from first principles. Admittedly, much work has been left for the future. For example, interesting as it would be, we have not attempted here to solve the slow evolution problem for more general wavenumber distributions. The singular nature of the asymptotic problem renders the task overly demanding from a numerical point of view. Moreover, the question of how the constant in the asymptotic formulation equivalent to the Kármán constant might be fixed was not addressed. The matching problem of the present logarithmic layer solution with the wall, buffer and wake layers seems to be the most important remaining unresolved problem. The problem might also reveal the dependence of the thickness L on the Reynolds number.

Acknowledgements. This research was supported by Australian Research Council's Discovery Early Career Researcher Award DE170100171 and Discovery Project DP170104703.

Declaration of interests. The authors report no conflict of interest.

Author ORCIDs.
Hugh M. Blackburn https://orcid.org/0000-0003-3469-5237;
Kengo Deguchi https://orcid.org/0000-0002-3709-3242;
Philip Hall https://orcid.org/0000-0001-5175-3115.

Appendix A. The jumps across the critical layer

It is sufficient to analyse the wave with $n = 0$; hereafter we omit the superscript (n) appearing in the expansion (4.4). Without loss of generality, we can set $\Phi_0 = 0$. The functions (u_w, v_w, w_w, p_w) are expanded as

$$u_w = \frac{\epsilon \Theta_Y}{\delta} \frac{\rho_p}{\overline{u}_Y} E\{u_{1w}(\Phi, Y, Z) + \delta u_{2w}(\Phi, Y, Z) + \cdots\} + \text{c.c.}, \tag{A1a}$$

$$v_w = \frac{\epsilon \Theta_Y}{\delta} \frac{\rho_p}{\overline{u}_Y} E\{v_{1w}(\Phi, Y, Z) + \delta v_{2w}(\Phi, Y, Z) + \cdots\} + \text{c.c.}, \tag{A1b}$$

$$w_w = \frac{\epsilon \Theta_Y}{\delta}\frac{\rho_p}{\overline{u}_Y} E\{w_{1w}(\Phi, Y, Z) + \delta w_{2w}(\Phi, Y, Z) + \cdots\} + \text{c.c.}, \tag{A1c}$$

$$p_w = \rho_p E\{p_{1w}(\Phi, Y, Z) + \delta p_{2w}(\Phi, Y, Z) + \cdots\} + \text{c.c.}, \tag{A1d}$$

where $\delta = \epsilon^{2/5}$ is the typical scale of the vertical cell depth measured in the Y coordinate (so the depth measured in y is $O(\epsilon^{-3/5})$). Here, for the sake of clarity, the wave pressure amplitude ρ_p is not rescaled to be an $O(\epsilon^0)$ quantity. We shall shortly see that the amplitude can be fixed through the roll–wave balance within the critical layer.

Around $Y = Y_0$, the mean flow can be approximated as

$$\overline{u}(Y) - \overline{u}(Y_0) \approx \delta \frac{\overline{u}_Y}{\Theta_Y}\{\Phi + \delta q \Phi^2 + \cdots\}, \tag{A2}$$

where $q(Z)$ is $(2\Theta_Y)^{-1}[(\overline{u}_{YY}/\overline{u}_Y) - (\Theta_{YY}/\Theta_Y)]$ evaluated at $Y = Y_n$. The convective operator $\partial_t + u\partial_x$ acting on the wave becomes

$$\mathrm{i}\alpha^{\dagger}\overline{u}_Y\{(\Phi + U_1) + \delta(q\Phi^2 + U_2) + \cdots\}, \tag{A3}$$

while the viscous operator becomes

$$\left(\frac{\epsilon\Theta_Y}{\delta}\right)^2 (\partial_X^2 + \partial_\Phi^2 + \partial_Z^2) + \cdots. \tag{A4}$$

Thus, in the majority of the flow the viscous effect is subdominant in the wave equations and, thus, they can be reduced to the Rayleigh equation (2.7*e*).

However, near the critical level where $(\Phi + U_1)$ vanishes, we must retain the viscous term. The balance of (A3) and (A4) suggests that the 'effective Reynolds number' R_{eff} of the wave equations can be found as $R_{\mathrm{eff}} = \overline{u}_Y(\epsilon\Theta_Y/\delta)^{-2}$. Thus, the critical layer thickness measured in y can be found as

$$\Delta \equiv R_{\mathrm{eff}}^{-1/3} = O((\epsilon/\delta)^{2/3}). \tag{A5}$$

For the distinguished limit $\delta = \epsilon^{2/5}$, we have $\Delta = \epsilon^{2/5}$. (Recall that δ is the relative thickness of the cell depth. In terms of y, the critical layer thickness Δ is thinner than the cell depth δ/ϵ.) In the following, δ/Δ is unity but we leave it as is in order to clarify the derivation.

For the mirror-symmetry mode, the critical layer becomes flat and sits at $Y = Y_n$. The symmetry of that mode implies that, with respect to the $\Phi = 0$ axis, U_1, V_1 are odd, and P_1, W_1, p_{1w} are even (in addition, p_{1w} is purely real). The next order components have opposite parity; for example, U_2, V_2 are even, P_2, W_2 are odd.

Now we analyse the flow around the critical level $\Phi = 0$. The local expansion of the streaks around the critical level can be found as

$$\Phi + U_1 = \lambda_1 \Phi + \cdots, \quad \delta(q\Phi^2 + U_2) = \lambda_0 + \cdots, \tag{A6a,b}$$

where

$$\lambda_1 = (1 + U_{1\Phi}|_{\Phi=0}), \quad \lambda_0 = U_2|_{\Phi=0}. \tag{A7a,b}$$

In terms of the stretched normal variable $\mathcal{N} = \Delta^{-1}\Phi$, the z component of the roll expands

$$W_1 = W_{10} + \Delta W_{11}(\mathcal{N}, Z) + \cdots, \quad W_2 = W_{20}(\mathcal{N}, Z) + \cdots. \tag{A8a}$$

Also, the inner wave expansions are

$$w_{1w} = \Delta^{-1} w_{10}(\mathcal{N}, Z) + \cdots, \quad w_{2w} = \Delta^{-2} w_{20}(\mathcal{N}, Z) + \cdots, \tag{A8b}$$

$$p_{1w} = p_{10}(Z) + \cdots, \quad p_{2w} = \Delta p_{20}(\mathcal{N}, Z) + \cdots. \tag{A8c}$$

Within the critical layer, the spanwise wave equation becomes

$$\begin{aligned} 0 = {} & \{\mathrm{i}\alpha^\dagger \lambda_1 \mathcal{N} w_{10} + \beta^\dagger p_{10Z} - w_{10\mathcal{N}\mathcal{N}}\} \\ & + \frac{\delta}{\Delta}\{\mathrm{i}\alpha^\dagger(\lambda_1 \mathcal{N} w_{20} + \lambda_0 w_{10}) - w_{20\mathcal{N}\mathcal{N}}\} + \cdots. \end{aligned} \tag{A9}$$

To find the jump we must solve the wave equation. We introduce a new variable $\zeta = (\mathrm{i}\alpha^\dagger \lambda_1)^{1/3}\mathcal{N}$ and a function

$$S(\zeta) = -\mathrm{i}^{2/3} \int_0^\infty \exp\left(-\frac{t^3}{3} - \mathrm{i}^{2/3}\zeta t\right) \mathrm{d}t \tag{A10}$$

that satisfies $S'' - \zeta S = 1$ and $S \to -\zeta^{-1}$ for $\mathcal{N} \to \pm\infty$. Then (A9) can be solved as

$$w_{10} = \frac{\beta^\dagger p_{10Z}}{(\mathrm{i}\alpha^\dagger \lambda_1)^{2/3}} S(\zeta), \quad w_{20} = \frac{\mathrm{i}\alpha^\dagger \lambda_0 \beta^\dagger p_{10Z}}{(\mathrm{i}\alpha^\dagger \lambda_1)^{4/3}} S'(\zeta). \tag{A11a,b}$$

In the z component of the roll equation, the critical layer balance is like $w_{yy} \approx (w^2)_z$, where the roll component contributes to the left-hand side and the wave component contributes to the right-hand side. Using the critical layer expansions (A8),

$$\begin{aligned} & \left(\frac{\epsilon \Theta_Y}{\delta}\right)^3 \Delta^{-1}(W_{11\mathcal{N}\mathcal{N}} + \frac{\delta}{\Delta} W_{20\mathcal{N}\mathcal{N}}) \\ & \quad \approx \frac{\rho_p^2}{\overline{u}_Y^2 \Delta^2} \left(\frac{\epsilon \Theta_Y}{\delta}\right)^3 2\beta^\dagger (|w_{10}|^2 + \frac{\delta}{\Delta}\{w_{10} w_{20}^* + w_{10}^* w_{20}\})_Z. \end{aligned}$$

Here by setting

$$\rho_p = \overline{u}_Y \Delta^{1/2} = \rho \overline{u}_Y^{5/6} \left(\frac{\epsilon \Theta_Y}{\delta}\right)^{1/3}, \tag{A12}$$

the balance is achieved and so we get the wave pressure expansion (4.4*e*) from (A1*d*). Using the solutions (A11*a*,*b*), the jumps can be obtained as

$$[W_{1\mathcal{N}}]_-^+ = \int_{-\infty}^{\infty} 2\{|w_{10}|^2\}_Z \mathrm{d}\mathcal{N} = \beta^\dagger \left\{\frac{n_0 \rho^2 \beta^{\dagger 2} |p_{10Z}|^2}{(\alpha^{\dagger 2}\lambda_1)^{5/3}}\right\}_Z, \tag{A13a}$$

$$\begin{aligned} [W_2]_-^+ &= \int_{-\infty}^{\infty} \int_{-\infty}^{\mathcal{N}_*} 2\{w_{10} w_{20}^* + w_{10}^* w_{20}\}_Z \mathrm{d}\mathcal{N} \mathrm{d}\mathcal{N}_* \\ &= \beta^\dagger \left\{\frac{\lambda_0}{\lambda_1} \frac{n_0 \rho^2 \beta^{\dagger 2} |p_{10Z}|^2}{(\alpha^{\dagger 2}\lambda_1)^{5/3}}\right\}_Z, \end{aligned} \tag{A13b}$$

where n_0 is the constant defined in (2.9*a*,*b*). From those results we arrive at the conditions (2.10*a*–*c*) and (4.10).

References

Adrian, R.J., Meinhart, C.D. & Tomkins, C.D. 2000 Vortex organization in the outer region of the turbulent boundary layer. *J. Fluid Mech.* **422**, 1–54.

Bakken, O.M., Krogstad, P.-A., Ashrafian, A. & Andersson, H.I. 2005 Reynolds number effects in the outer layer of the turbulent flow in a channel with rough walls. *Phys. Fluids* **17** (6), 065101.

Batchelor, G.K. 1956 On steady laminar flow with closed streamlines at large Reynolds number. *J. Fluid Mech.* **1** (2), 177–190.

Batchelor, G.K. 1967 *An Introduction to Fluid Dynamics*. Cambridge University Press.

Beaume, C., Chini, G.P., Julien, K. & Knobloch, E. 2015 Reduced description of exact coherent states in parallel shear flows. *Phys. Rev.* E **91**, 043010.

Beaume, C., Knobloch, E., Chini, G.P. & Julien, K. 2016 Modulated patterns in a reduced model of a transitional shear flow. *Phys. Scr.* **91**, 024003.

Benney, D.J. & Chow, K. 1989 A mean flow first harmonic theory for hydrodynamic instabilities. *Stud. Appl. Maths* **80** (1), 37–83.

Blackburn, H.M., Hall, P. & Sherwin, S.J. 2013 Lower branch equlibria in Couette flow: the emergence of canonical states for arbitrary shear flows. *J. Fluid Mech.* **721**, 58–85.

Brandenburg, A., Norlund, A., Stein, R.F. & Torkelsson, U. 1995 Dynamo-generated turbulence and large-scale magnetic fields in a Keplerian shear flow. *Astrophys. J.* **446**, 741–754.

Chernyshenko, S.I. & Baig, M.F. 2005 The mechanism of streak formation in near-wall turbulence. *J. Fluid Mech.* **544**, 99–131.

Chini, G.P., Montemuro, B., White, C.M. & Klewicki, J. 2017 A self-sustaining process model of inertial layer dynamics in high Reynolds number turbulent wall flows. *Phil. Trans. R. Soc.* A **375**, 20160090.

Chung, D., Monty, J. & Ooi, A. 2014 An idealised assessment of Townsend's outer-layer similarity hypothesis for wall turbulence. *J. Fluid Mech.* **742**, R3.

Clever, R.M. & Busse, F.H. 1992 Three-dimensional convection in a horizontal fluid layer subjected to a constant shear. *J. Fluid Mech.* **234**, 511–527.

Cossu, C. & Hwang, Y. 2017 Self-sustaining processes at all scales in wall-bounded turbulent shear flows. *Phil. Trans. R. Soc.* A **375**, 20160088.

Deguchi, K. 2015 Self-sustained states at Kolmogorov microscale. *J. Fluid Mech.* **781**, R6.

Deguchi, K. 2019 Inviscid instability of a unidirectional flow sheared in two transverse directions. *J. Fluid Mech.* **874**, 979–994.

Deguchi, K. & Hall, P. 2014*a* Canonical exact coherent structures embedded in high Reynolds number flows. *Phil. Trans. R. Soc.* A **372** (2020), 20130352.

Deguchi, K. & Hall, P. 2014*b* Free-stream coherent structures in parallel boundary-layer flows. *J. Fluid Mech.* **752**, 602–625.

Deguchi, K. & Hall, P. 2014*c* The high-Reynolds-number asymptotic development of nonlinear equilibrium states in plane Couette flow. *J. Fluid Mech.* **750**, 99–112.

Deguchi, K. & Hall, P. 2016 On the instability of vortex–wave interaction states. *J. Fluid Mech.* **802**, 634–666.

Deguchi, K., Hall, P. & Walton, A. 2013 The emergence of localized vortex–wave interaction states in plane Couette flow. *J. Fluid Mech.* **721**, 58–85.

Eckhardt, B. & Zammert, S. 2018 Small scale exact coherent structures at large Reynolds numbers in plane Couette flow. *Nonlinearity* **31** (2), R66–R77.

Faisst, H. & Eckhardt, B 2003 Traveling waves in pipe flow. *Phys. Rev. Let.* **91** (22), 224502.

Flores, O. & Jiménez, J. 2006 Effect of wall-boundary disturbances on turbulent channel flows. *J. Fluid Mech.* **566**, 357–376.

Gerz, T., Schumann, U. & Elgobashi, S.E. 1989 Direct numerical simulation of stratified homogeneous shear flows. *J. Fluid Mech.* **200**, 563–594.

Gibson, J.F. & Brand, E. 2014 Spatially localized solutions of planar shear flow. *J. Fluid Mech.* **745**, 25–61.

Gibson, J.F., Halcrow, J. & Cvitanović, P. 2008 Visualizing the geometry of state space in plane Couette flow. *J. Fluid Mech.* **611**, 1–24.

Gibson, J.F., Halcrow, J. & Cvitanović, P. 2009 Equilibrium and travelling-wave solutions of plane Couette flow. *J. Fluid Mech.* **638**, 243–266.

Gómez, F., Pérez, J.M., Blackburn, H.M. & Theofilis, V. 2015 On the use of matrix-free shift-invert strategies for global flow instability analysis. *Aerosp. Sci. Technol.* **44**, 69–76.

Hall, P. 2018 Vortex–wave interaction arrays: a sustaining mechanism for the log layer? *J. Fluid Mech.* **850**, 46–82.

Hall, P. & Lakin, W 1988 The fully nonlinear development of Görtler vortices in growing boundary layers. *Proc. R. Soc. Lond.* A **415**, 421–44.

HALL, P. & SHERWIN, S.J. 2010 Streamwise vortices in shear flows: harbingers of transition and the skeleton of coherent structures. *J. Fluid Mech.* **661**, 178–205.
HALL, P. & SMITH, F.T. 1988 The nonlinear interaction of Tollmein–Schlichting waves and Taylor–Görtler vortices in curved channel flows. *Proc. R. Soc. Lond.* A **417**, 255–282.
HALL, P. & SMITH, F.T. 1991 On strongly nonlinear vortex/wave interactions in boundary-layer transition. *J. Fluid Mech.* **227**, 641–666.
HAMILTON, J.M., KIM, J. & WALEFFE, F. 1995 Regeneration mechanisms of near-wall turbulence structures. *J. Fluid Mech.* **287**, 317–348.
HAWLEY, J.F., GAMMIE, C.F. & BALBUS, S.A. 1995 Local three-dimensional magnetohydrodynamic simulations of acretion disks. *Astrophys. J.* **440**, 792.
HUTCHINS, N. & MARUSIC, I. 2007 Evidence of very long meandering features in the logarithmic region of turbulent boundary layers. *J. Fluid Mech.* **579**, 1–29.
HWANG, Y. 2015 Statistical structure of self-sustaining attached eddies in turbulent channel flow. *J. Fluid Mech.* **767**, 254–289.
HWANG, Y. & COSSU, C. 2011 Self-sustained processes in the logarithmic layer of turbulent channel flows. *Phys. Fluids* **23** (6), 061702.
ITANO, T. & GENERALIS, S.C. 2009 Hairpin vortex solution in planar Couette flow: a tapestry of knotted vortices. *Phys. Rev. Let.* **102**, 114501.
ITANO, T. & TOH, S. 2001 The dynamics of bursting process in wall turbulence. *J. Phys. Soc. Japan* **70** (3), 703–716.
JIMÉNEZ, J. 2013 How linear is wall turbulence? *Phys. Fluids* **25**, 110814.
JIMÉNEZ, J. & MOIN, P. 1991 The minimal flow unit in near-wall turbulence. *J. Fluid Mech.* **225**, 213–240.
JIMÉNEZ, J. & PINELLI, A. 1999 The autonomous cycle of near-wall turbulence. *J. Fluid Mech.* **389**, 335–359.
KALTENBACH, H.-J., GERZ, T. & SCHUMANN, U. 1994 Large-eddy simulation of homogeneous turbulence and diffusion in a stably stratified shear flow. *J. Fluid Mech.* **280**, 1–40.
VON KÁRMÁN, T.. 1930 Mechanische Ähnichkeit und Turbulenz. *Nach. Akad. Wiss. Gött.: Math.-Phys. Klasse* **58**, 58–76.
KAWAHARA, G., UHLMANN, M. & VAN VEEN, L. 2012 The significance of simple invariant solutions in turbulent flows. *Annu. Rev. Fluid Mech.* **44**, 203–225.
KIDA, S. & TANAKA, M. 1994 Dynamics of vortical structures in a homogeneous shear flow. *J. Fluid Mech.* **274**, 43–68.
KIM, H.T., KLINE, S.J. & REYNOLDS, W.C. 1971 The production of turbulence near a smooth wall in a turbulent boundary layer. *J. Fluid Mech.* **50** (1), 133–160.
KLEWICKI, J. 2013 A description of turbulent wall-flow vorticity consistent with mean dynamics. *J. Fluid Mech.* **737**, 176–204.
KLEWICKI, J. & OBERLACK, M. 2015 Finite Reynolds number properties of a turbulent channel flow similarity solution. *Phys. Fluids* **27**, 095110.
KLEWICKI, J., PHILIP, J., MARUSIC, I., CHAUHAN, K. & MORRILL-WINTER, C. 2014 Self-similarity in the inertial region of wall turbulence. *Phys. Rev.* E **90**, 063015.
LASKARI, A., DE KAT, R., HEARST, R.J. & GANAPATHISUBRAMANI, B. 2018 The evolution of uniform momentum zones in a turbulent boundary layer. *J. Fluid Mech.* **842**, 554–590.
LOZANO-DURÁN, A. & BAE, H.J. 2019 Characteristic scales of Townsend's wall-attached eddies. *J. Fluid Mech.* **868**, 698–725.
MALKUS, W.V.R. 1956 Outline of a theory of turbulent shear flow. *J. Fluid Mech.* **1** (5), 521–39.
MARUSIC, I. & MONTY, J.P. 2019 Attached eddy model of wall turbulence. *Annu. Rev. Fluid Mech.* **51**, 49–74.
MCKEON, B.J. & SHARMA, A.S. 2010 A critical layer framework for turbulent pipe flow. *J. Fluid Mech.* **658**, 336–382.
MEINHART, C.D. & ADRIAN, R.J. 1995 On the existence of uniform momentum zones in a turbulent boundary layer. *Phys. Fluids* **7** (7), 694–696.
MILLIKAN, C.B. 1938 A critical discussion of turbulent flows in channels and tubes. In *Proceedings of the 5th International Congress for Applied Mechanics* (ed. J. P. Den Hartog & H. Peters), pp. 386–392, Wiley.
MIZUNO, Y. & JIMÉNEZ, J. 2013 Wall turbulence without walls. *J. Fluid Mech.* **723**, 429–455.
MOARREF, R., SHARMA, A.S., TROPP, J.A. & MCKEON, B.J. 2013 Model-based scaling of the streamwise energy density in high-Reynolds-number turbulent channels. *J. Fluid Mech.* **734**, 275–316.
MONTEMURO, B., WHITE, C.M., KLEWICKI, J. & CHINI, G.P. 2020 A self-sustaining process theory for uniform momentum zones and internal shear layers in high Reynolds number shear flows. *J. Fluid Mech.* **901**, A28.
MORRILL-WINTER, C., PHILIP, J. & KLEWICKI, J. 2017 An invariant representation of mean inertia: theoretical basis for the log layer in turbulent boundary layers. *J. Fluid Mech.* **813**, 594–617.

NAGATA, M. 1990 Three-dimensional finite-amplitude solutions in plane Couette flow: bifurcation from infinity. *J. Fluid Mech.* **217**, 519–527.
PERRY, A.E. & CHONG, M.S. 1982 On the mechanism of wall turbulence. *J. Fluid Mech.* **119**, 173–217.
PERRY, A.E. & MARUSIC, I. 1995 A wall-wake model for the turbulence structure of boundary layers. Part 1. Extension of the attached eddy hypothesis. *J. Fluid Mech.* **298**, 361–388.
PUMIR, A. 1996 Turbulence in homogeneous shear flows. *Phys. Fluids* **8** (11), 3112–3127.
RIOLS, A., RINCON, F., COSSU, C., LESUR, G., LONGARETTI, P.-Y., OGILVIE, G.I. & HERAULT, J. 2013 Global bifurcations to subcritical magnetorotational dynamo action in Keplerian shear flow. *J. Fluid Mech.* **731**, 1–45.
ROBINSON, J.L. 1967 Finite amplitude convection cells. *J. Fluid Mech.* **30** (3), 577–600.
ROGALLO, R.S. 1981 Numerical experiments in homogeneous turbulence. *NASA Tech. Memorandum* 81315.
ROGERS, M.M. & MOIN, P. 1987 The structure of the vorticity field in homogeneous turbulent flows. *J. Fluid Mech.* **176**, 33–66.
SCHNEIDER, T., GIBSON, J.F. & BURKE, J. 2010*a* Snakes and ladders: localized solutions of plane Couette flow. *Phys. Rev. Let.* **104** (10), 104501.
SCHNEIDER, T.M., MARINC, D. & ECKHARDT, B. 2010*b* Localised edge states nucleate turbulence in extended plane Couette cells. *J. Fluid Mech.* **646**, 441–451.
SCHOPPA, W. & HUSSAIN, F. 2002 Coherent structure generation in near-wall turbulence. *J. Fluid Mech.* **453**, 57–108.
SCHUMANN, U. 1985 Algorithms for direct numerical simulation of shear-periodic turbulence. In *Ninth International Conference on Numerical Methods in Fluid Dynamics* (ed. Soubbaramayer & J. P. Boujot), *Lecture Notes in Physics*, vol. 218, pp. 492–496. Springer.
SEKIMOTO, A., DONG, S. & JIMÉNEZ, J. 2016 Direct numerical simulation of statistically stationary and homogeneous shear turbulence and its relation to other shear flows. *Phys. Fluids* **26** (3), 035101.
SEKIMOTO, A. & JIMÉNEZ, J. 2017 Vertically localised equlibrium solutions in large-eddy simulations of homogeneous shear flow. *J. Fluid Mech.* **827**, 225–249.
DE SILVA, C.M., HUTCHINS, N. & MARUSIC, I. 2016 Uniform momentum zones in turbulent boundary layers. *J. Fluid Mech.* **786**, 309–321.
DE SILVA, C.M., PHILIP, J., HUTCHINS, N. & MARUSIC, I. 2017 Interfaces of uniform momentum in turbulent boundary layers. *J. Fluid Mech.* **820**, 451–478.
THOMAS, V.L., LIEU, B.K., JOVANOVIĆ, M.R., FARRELL, B.F., IOANNOU, P.J. & GAYME, D.F. 2014 Self-sustaining turbulence in a restricted nonlinear model of plane Couette flow. *Phys. Fluids* **26**, 105112.
TOWNSEND, A.A. 1951 The structure of the turbulent boundary layer. *Math. Proc. Camb. Phil. Soc.* **47**, 375–395.
TOWNSEND, A.A. 1976 *The Structure of Turbulent Shear Flow*, 2nd edn. Cambridge University Press.
WALEFFE, F. 1997 On a self-sustaining process in shear flows. *Phys. Fluids* **9**, 883–890.
WALEFFE, F. 1998 Three-dimensional coherent states in plane shear flows. *Phys. Rev. Let.* **81** (19), 4140–4143.
WALEFFE, F. 2003 Homotopy of exact coherent structures in plane shear flows. *Phys. Fluids* **15** (6), 1517–1534.
WANG, J., GIBSON, J.F. & WALEFFE, F. 2007 Lower branch coherent states in shear flows: transition and control. *Phys. Rev. Let.* **98** (20), 204501.
WEDIN, H. & KERSWELL, R.R. 2004 Exact coherent structures in pipe flow: travelling wave solutions. *J. Fluid Mech.* **508**, 333–371.
WEI, W., FIFE, P., KLEWICKI, J. & MCMURTRY, P. 2005 Properties of the mean momentum balance in turbulent boundary layer, pipe and channel flows. *J. Fluid Mech.* **522**, 303–327.
WILLIS, A.P., CVITANOVIĆ, P. & AVILA, M. 2013 Revealing the state space of turbulent pipe flow by symmetry reduction. *J. Fluid Mech.* **721**, 514–540.
YANG, Q., WILLIS, A.P. & HWANG, Y. 2018 Energy production and self-sustained turbulence at the Kolmogorov scale in Couette flow. *J. Fluid Mech.* **834**, 531–554.
YANG, Q., WILLIS, A.P. & HWANG, Y. 2019 Exact coherent states of attached eddies in channel flow. *J. Fluid Mech.* **862**, 1029–1059.